

Role of the high-spin nucleon and delta resonances in the $K\Lambda$ and $K\Sigma$ photoproduction off the nucleon

N. H. Luthfiah and T. Mart*

Departemen Fisika, FMIPA, Universitas Indonesia, Depok 16424, Indonesia

We have investigated the effect of nucleon and delta resonances with spins 11/2, 13/2, and 15/2 in the kaon photoproduction process $\gamma + N \rightarrow K + Y$ by using two covariant isobar models. The formalism for high-spin propagators and interaction Lagrangians were adopted from the works of Pascalutsa and Vrancx *et al.* The calculated scattering amplitudes were decomposed into six Lorentz- and gauge-invariant matrices, from which we calculated the cross sections and polarization observables. The unknown parameters in the amplitudes, i.e., the coupling constants and hadronic form factor cutoffs, were obtained by fitting the calculated observables to experimental data. In the $K\Lambda$ channels the inclusion of $N(2600)I_{1,11}$ and $N(2700)K_{1,13}$ resonances improves the agreement between model calculations and experimental data significantly and reduces the dominance of resonances in the model by increasing the hadronic form factor cutoff of the Born terms. Furthermore, the inclusion of these resonances reduces the number of resonance structures in cross sections, including the structure in the $K^0\Lambda$ differential cross section at $W \approx 1650$ MeV, which could become a hint of the narrow resonance. In the $K\Sigma$ channels the inclusion of $N(2600)I_{1,11}$, $N(2700)K_{1,13}$, $\Delta(2420)H_{3,11}$, $\Delta(2750)I_{3,13}$, and $\Delta(2950)K_{3,15}$ states also significantly improves the model and increases the hadronic form factor cutoff of the Born terms. However, different from the $K\Lambda$ channels, the inclusion of these high-spin resonances leads to more resonance structures in the $K^+\Sigma^0$ differential cross section. This investigation reveals that the second and third peaks in the $K^+\Sigma^0$ differential cross section originate from the $\Delta(2000)F_{35}$ and $N(2290)G_{19}$ resonances, respectively. We have also evaluated the resonance properties at the pole positions and using the Breit-Wigner method. In both $K\Lambda$ and $K\Sigma$ channels the inclusion of the high-spin baryon resonances was found to improve the agreement between the resonance properties obtained in this study and those listed by the Particle Data Group.

PACS numbers: 13.60.Le, 14.20.Gk, 25.20.Lj

I. INTRODUCTION

Recently, the effect of spins-7/2 and -9/2 nucleon resonances on kaon photoproduction processes has been phenomenologically investigated by using a covariant isobar model [1], in which the scattering amplitude was calculated by using the appropriate Feynman diagrams depicted in Fig. 1. The analytical calculation performed in this study made use of the consistent interaction Lagrangians proposed by Pascalutsa [2]. The calculated observables were fitted to nearly 7400 experimental data points. The result of the fitting process showed that the inclusion of spins-7/2 and 9/2 nucleon resonances could improve the agreement between the model calculation and the experimental data. The model was later extended to describe both $\gamma p \rightarrow K^+\Lambda$ and $\gamma n \rightarrow K^0\Lambda$ processes, simultaneously [3]. In the latter, the model was fitted to nearly 9400 data points, including recent data from the CLAS and MAMI collaborations. The extended model yielded a nice agreement between the calculated observables and experimental data in both isospin channels.

Despite the success of the model, it has not yet consider the resonances with spins-11/2, 13/2 and 15/2, which

are tabulated by the Particle Data Group (PDG) listing [4] (see Table I). Given the fact that the inclusion of spins-7/2 and 9/2 resonances in Ref. [1] significantly improves the model, we could also expect that a similar phenomenon would be obtained with the inclusion of the resonances listed in Table I. Furthermore, we can also extend the model to include the four $K\Sigma$ isospin channels, i.e. $K^+\Sigma^0$, $K^0\Sigma^+$, $K^+\Sigma^-$ and $K^0\Sigma^0$ channels. Since the total isospin of these channels is 3/2, the Δ resonances are allowed as the intermediate states. An isobar model for $K\Sigma$ reaction can be constructed from the well-known $K\Lambda$ model based on our previous studies, e.g., in Ref. [5]. For the $K\Lambda$ final states, the isospin symmetry couples the $K^+\Lambda$ and $K^0\Lambda$ channels, whereas for the $K\Sigma$ final states, the $K^+\Sigma^0$, $K^0\Sigma^+$, $K^+\Sigma^-$, and $K^0\Sigma^0$ production processes are coupled by isospin symmetry to one model. As mentioned above, there are nearly 9400 data points available for the $K\Lambda$ channels, and nearly 8000 data points for $K\Sigma$ ones. These data sets will be fitted to the $K\Lambda$ and $K\Sigma$ models separately. In principle, all six isospin channels can also be coupled, since all $K\Lambda$ and $K\Sigma$ isospin channels utilize the same leading Born coupling constants, i.e., the $g_{K\Lambda N}$ and $g_{K\Sigma N}$. However, since we have fixed these coupling constants to the SU(3) values [6], the $K\Lambda$ and $K\Sigma$ channels are naturally decoupled.

To the best of our knowledge, there are limited studies investigating the contribution of high-spin nucleon and delta resonances in kaon photoproduction with the field-

*Corresponding author: terry.mart@sci.ui.ac.id

theoretic model. Presumably, this is due to the complicated formulations of propagator and vertex factors along with the problem of lower-spin background that plagued the formulation of high-spin ($J > 1/2$) resonance propagator. Therefore, the first purpose of this paper is to set forth the formulation of higher-spin resonances amplitude. After that we can study their effect on the six isospin channels of kaon photoproduction (see Table II) by means of a covariant isobar model.

We have organized this paper as follows. In Sec. II we present the formalism used in our study. In Sec. III we present the numerical result and discuss the comparison between model calculations and experimental data. Finally, in Sec. IV we summarize and conclude our work. The extracted form functions used to calculate the observables for the fitting process are given in Appendix A.

II. FORMALISM

As mentioned above we adopt the formalism of the nucleon propagators and the interaction Lagrangian developed by Pascalutsa [2] and Vrancx *et al.* [7]. In our previous work, we explained this formalism in details and constructed the reaction amplitude for the nucleon resonances with spins 7/2 and 9/2 [1]. To facilitate the reader, in this section we briefly discuss this formalism and derive the construction of the spins-11/2, -13/2, and -15/2 resonance propagators along with their interaction Lagrangians. A preliminary result for the analytical form of the production amplitudes involving nucleon resonances with spins up to 13/2 has been reported in a conference [8]. The notation of the four-momentum of photon, nucleon, kaon, and hyperon used in the following discussion is given in the caption of Fig. 1, with $p_R = p + k = p_Y + q$.

A. Consistent Interaction Theory

A consistent interaction Lagrangian is required to eliminate the appearance of the lower-spin background amplitude, which is known as an intrinsic problem in the

TABLE I: Nucleon and delta resonances with spins from 11/2 to 15/2 used in our study and tabulated by the PDG in their particle listing [4].

Resonance	J^P	Status	Mass (MeV)	Width (MeV)
$N(2600)I_{1,11}$	$11/2^-$	***	2600 ± 50	650 ± 150
$N(2700)K_{1,13}$	$13/2^+$	**	2612 ± 45	350 ± 50
$\Delta(2420)H_{3,11}$	$11/2^+$	****	2450 ± 150	500 ± 200
$\Delta(2750)I_{3,13}$	$13/2^-$	**	2794 ± 80	350 ± 100
$\Delta(2950)K_{3,15}$	$15/2^+$	**	2990 ± 100	330 ± 100

TABLE II: Six possible isospin channels of kaon photoproduction on the nucleon along with their threshold energies in terms of photon lab energy $k^{\text{thr.}}$ and total c.m. energy $W^{\text{thr.}}$.

No.	Reactions	$k^{\text{thr.}}$ (MeV)	$W^{\text{thr.}}$ (MeV)
1)	$\gamma + p \rightarrow K^+ + \Lambda$	911	1609
2)	$\gamma + n \rightarrow K^0 + \Lambda$	915	1613
3)	$\gamma + p \rightarrow K^+ + \Sigma^0$	1046	1686
4)	$\gamma + p \rightarrow K^0 + \Sigma^+$	1048	1687
5)	$\gamma + n \rightarrow K^+ + \Sigma^-$	1052	1691
6)	$\gamma + n \rightarrow K^0 + \Sigma^0$	1051	1690

Rarita-Schwinger (R-S) formulation of the spin-3/2 (or higher) propagator. A number of solutions have been put forward to solve this problem in the last decades. Among them, those of Pascalutsa [2] and Vrancx *et al.* [7] are relevant to our present work. They constructed the interaction Lagrangians which automatically cancel out the lower spin contributions to the scattering amplitude. Pascalutsa proposed a gauge-invariant interaction structure for spin-3/2 particles by introducing a local symmetry to the R-S field $\psi_{\mu_1 \dots \mu_n}$. The local symmetry reads [7]

$$\psi_{\mu_1 \dots \mu_n} \rightarrow \psi_{\mu_1 \dots \mu_n} + \frac{1}{n(n-1)!} \sum_{P(\mu)} \partial_{\mu_1} \xi_{\mu_2 \dots \mu_n}, \quad (1)$$

where the totally symmetric and space-time dependent tensor-spinor field $\xi_{\mu_2 \dots \mu_n}$ fulfills

$$\gamma^{\mu_1} \xi_{\mu_1 \mu_2 \dots \mu_{n-1}} = 0. \quad (2)$$

To construct a consistent interaction Lagrangian for particles with spin-3/2 we need a gauge-invariant field $G_{\mu\nu}$, taken from Ref. [2], and the interaction operator $O_{(\mu,\nu)\lambda}^{(3/2)}$, adopted from Ref. [7]. The invariant field and the interaction operator is written in the form of

$$\begin{aligned} G_{\mu\nu} &= \partial_\mu \psi_\nu - \partial_\nu \psi_\mu \\ &= (\partial_\mu g_{\nu\lambda} - \partial_\nu g_{\mu\lambda}) \psi^\lambda \\ &= O_{(\mu,\nu)\lambda}^{(3/2)} \psi^\lambda, \end{aligned} \quad (3)$$

with

$$O_{(\mu,\nu)\lambda}^{(3/2)} = (\partial_\mu g_{\nu\lambda} - \partial_\nu g_{\mu\lambda}), \quad (4)$$

where ψ_μ is the massive R-S field that obeys the R-S equation and its constraints. The interaction operator fulfills the following property,

$$\partial^\lambda O_{(\mu,\nu)\lambda}^{(3/2)}(\partial) = O_{(\mu,\nu)\lambda}^{(3/2)}(\partial) \partial^\lambda, \quad (5)$$

which maintains the invariance of $G_{\mu\nu}$ under the uR-S_{5/2} gauge as stated in Eq. (1). With the invariant field and spin-3/2 interaction operator, Vrancx *et al.* constructed

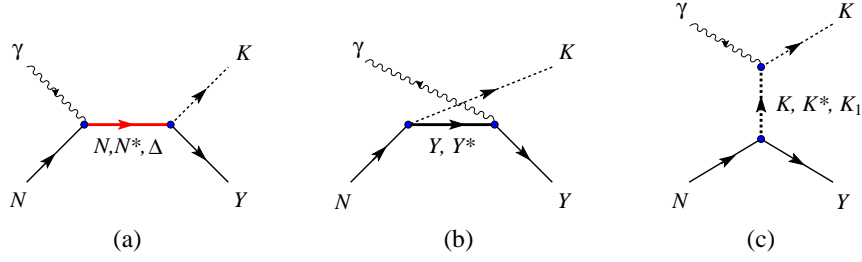


FIG. 1: Feynman diagrams of the kaon photoproduction $\gamma(k) + N(p) \rightarrow K(q) + Y(p_Y)$ for the (a) s -channel, (b) u -channel, and (c) t -channel intermediate states.

a consistent interaction theory for spin-5/2 field. This formulation is later expanded for general high-spin field. Vrancx *et al.* defined a general interaction operator as [7]

$$O_{(\mu_1 \dots \mu_n, \nu_1 \dots \nu_n) \lambda_1 \dots \lambda_n}^{(n+1/2)}(\partial) = \frac{1}{(n!)^2} \sum_{P(\nu)} \sum_{P(\lambda)} O_{(\mu_1, \nu_1) \lambda_1}^{(3/2)}(\partial) \dots O_{(\mu_n, \nu_n) \lambda_n}^{(3/2)}(\partial), \quad (6)$$

with $P(\mu)P(\lambda)$ indicate all possible permutations for all μ and λ . Vrancx reduced the indices of the $G_{\mu\nu}$ field introduced by Pascalutsa in Eq. (3), because the $G_{\mu\nu}$ field contains too many indices compared to the original field $\psi_{\mu_1 \dots \mu_n}$. A new field is introduced by Vrancx as $\Psi_{\mu} = O_{(\mu, \nu) \lambda}^{(3/2)} \psi^{\lambda} \gamma^{\nu}$. For particles with spin- $(n+1/2)$ the gauge-invariant field can be written as

$$\Psi_{\mu_1 \dots \mu_n} = O_{(\mu_1 \dots \mu_n, \nu_1 \dots \nu_n) \lambda_1 \dots \lambda_n}^{(n+1/2)}(\partial) \psi^{\lambda_1 \dots \lambda_n} \gamma^{\nu_1 \dots \nu_n}. \quad (7)$$

The interaction operator for the above field reads

$$\begin{aligned} O_{(\mu_1 \dots \mu_n) \lambda_1 \dots \lambda_n}^{(n+1/2)}(\partial) &= \gamma^{\nu_1 \dots \nu_n} O_{(\mu_1 \dots \mu_n, \nu_1 \dots \nu_n) \lambda_1 \dots \lambda_n}^{(n+1/2)}(\partial) \\ &= \frac{1}{(n!)^2} \sum_{P(\lambda)} O_{(\mu_1) \lambda_1}^{(3/2)}(\partial) \dots O_{(\mu_n) \lambda_n}^{(3/2)}(\partial), \end{aligned} \quad (8)$$

where

$$O_{(\mu_n) \lambda_n}^{(3/2)}(\partial) = \gamma^{\nu} O_{(\mu, \nu) \lambda}^{(3/2)}(\partial). \quad (9)$$

With this consistent interaction we are ready to construct the Lagrangians for high-spin interactions.

B. Interaction Lagrangians

The basic Lagrangian for the kaon-hyperon-nucleon interaction is

$$\mathcal{L}_{\text{had}} = g_{KYN} \bar{\Psi}_Y \gamma_5 \Psi_N \Phi_K. \quad (10)$$

Following this basic Lagrangian, the standard interaction Lagrangian for the interaction with spin-1/2 resonances is written as

$$\mathcal{L}_{\text{had}} = g_{KYR} \bar{\Psi}_Y \gamma_5 \Psi_R \Phi_K + \text{H.c.} \quad (11)$$

According to Pascalutsa the hadronic interaction Lagrangian for spin-3/2 resonance with mass m_R reads [9]

$$\mathcal{L}_{\text{had}} = \frac{g_{KYR}}{m_R^2} \epsilon^{\mu\nu\alpha\beta} \bar{\Psi}_Y \partial_{\beta} \phi^* \gamma_5 \gamma_{\alpha} (\partial_{\mu} \psi_{\nu}) + \text{H.c.}, \quad (12)$$

where $\bar{\Psi}_Y$ is the spinor field of the hyperon, ϕ is the pseudoscalar field of the kaon, and ψ_{ν} is the massive R-S field of the nucleon or resonance. However, the above Lagrangian is inconsistent for higher-spin resonances. With the substitution proposed by Vrancx, $\psi_{\mu} \rightarrow \bar{\Psi}_{\mu}/m_R$, the Lagrangian for a resonance with spin 3/2 can be written as

$$\mathcal{L}_{\text{had}} = \frac{g_{KYR}}{m_R^3} \epsilon^{\mu\nu\alpha\beta} \bar{\Psi}_Y \partial_{\beta} \phi^* \gamma_5 \gamma_{\alpha} \partial_{\mu} \Psi_{\nu} + \text{H.c.}, \quad (13)$$

whereas the Lagrangian for hadronic interaction with spin- $(n+1/2)$ resonances has the form of

$$\begin{aligned} \mathcal{L}_{\text{had}} &= \frac{g_{KYR}}{m_R^{2n+1}} \epsilon^{\mu\nu\alpha\beta} \partial^{\nu_1} \dots \partial^{\nu_{n-1}} \bar{\Psi}_Y \partial_{\beta} \phi^* \\ &\quad \times \gamma_5 \gamma_{\alpha} (\partial_{\mu} \Psi_{\nu_1 \dots \nu_n}) + \text{H.c} \\ &= \frac{g_{KYR}}{m_R^{2n+1}} \epsilon^{\mu\nu\alpha\beta} \bar{\Psi}_Y \partial_{\beta} \phi^* \gamma_5 \gamma_{\alpha} \\ &\quad \times \partial_{\mu} O_{(\mu_1 \dots \mu_n, \nu_1 \dots \nu_n) \lambda_1 \dots \lambda_n}^{(n+1/2)}(\partial) \\ &\quad \times \gamma^{\alpha_1} \dots \gamma^{\alpha_n} \psi^{\lambda_1 \dots \lambda_n} + \text{H.c.} \end{aligned} \quad (14)$$

In addition to the hadronic Lagrangian, Pascalutsa has also constructed the Lagrangian for the electromagnetic interaction, which is written as [10]

$$\begin{aligned} \mathcal{L}_{\text{em}} &= \frac{e}{m_R^3} \bar{\Psi}^{\beta} \left\{ (g_1 \epsilon_{\mu\nu\alpha\beta} \partial^{\alpha} \Psi + g_2 \gamma_5 g_{\beta\nu} \partial_{\mu} \Psi \right. \\ &\quad \left. + g_3 \gamma_{\mu} \gamma^{\rho} \epsilon_{\rho\nu\alpha\beta} \partial^{\alpha} \Psi + g_4 \gamma_5 \gamma_{\mu} \gamma^{\rho} \right. \\ &\quad \left. \times (\partial_{\rho} g_{\nu\beta} - \partial_{\nu} g_{\rho\beta}) \Psi \right\} F^{\mu\nu} + \text{H.c.}, \end{aligned} \quad (15)$$

where $F^{\mu\nu}$ is the conventional electromagnetic field strength tensor. To correctly model the interaction in discussion, a consistent interaction for the electromagnetic interaction Lagrangian is needed. The electromagnetic interaction Lagrangian for the resonance particles

with spin- $(n + 1/2)$ can be written as

$$\begin{aligned} \mathcal{L}_{\text{em}} = & \frac{e}{m_R^{2n+1}} \bar{\Psi}^{\beta_1 \dots \beta_n} \{ (g_1 \epsilon_{\mu\nu\alpha\beta_n} \partial^\alpha \Psi \\ & + g_2 \gamma_5 g_{\beta_n \nu} \partial_\mu \Psi + g_3 \gamma_\mu \gamma^\rho \epsilon_{\rho\nu\alpha\beta_n} \partial^\alpha \Psi \\ & + g_4 \gamma_5 \gamma_\mu \gamma^\rho (\partial_\rho g_{\nu\beta_n} - \partial_\nu g_{\rho\beta_n}) \Psi \} \\ & \times \partial_{\beta_1} \dots \partial_{\beta_{n-1}} F^{\mu\nu} + \text{H.c.} \end{aligned} \quad (16)$$

The consistency of the interaction is guaranteed by the operator interaction which fulfills:

$$p_R^{\lambda_i} O_{(\mu_1 \dots \mu_n, \nu_1 \dots \nu_n) \lambda_1 \dots \lambda_n}^{(n+1/2)}(p_R) = 0, \quad (17)$$

with $i = 1, 2, \dots, n$ and $p_R^{\lambda_i}$ is the four-momenta of the resonance particles with spin- $(n + 1/2)$.

The electromagnetic and hadronic vertices, which are required to calculate the scattering amplitude, can be obtained from the interaction Lagrangians constructed in the previous discussion. As the result the hadronic vertex can be written as

$$\begin{aligned} \Gamma_{\mu_1 \dots \mu_2}^{\text{had}} = & \frac{g_{KYR}}{m_R^{2n+1}} \epsilon^{\mu\nu\alpha\beta} p_\Lambda^{\nu_1} \dots p_\Lambda^{\nu_{n-1}} q_\beta \gamma_5 \gamma_\alpha p_{R\mu} \\ & \times O_{(\nu_1 \dots \nu_n, \alpha_1 \dots \alpha_n) \mu_1 \dots \mu_n}^{(n+1/2)}(p_R) \gamma^{\alpha_1} \dots \gamma^{\alpha_n}. \end{aligned} \quad (18)$$

and the electromagnetic vertex reads

$$\begin{aligned} \Gamma_{\nu_1 \dots \nu_n}^{\text{em}} = & \frac{e}{m_R^{2n+1}} O_{n+1/2}^{(\beta_1 \dots \beta_n, \alpha_1 \dots \alpha_n) \nu_1 \dots \nu_n}(p_R) \gamma_{\alpha_1} \dots \gamma_{\alpha_n} \\ & \times \left\{ g_1 \epsilon_{\mu\nu\alpha\beta_n} p^\alpha + g_2 \gamma_5 g_{\beta_n \nu} p_\mu \right. \\ & + g_3 \gamma_\mu \gamma^\rho \epsilon_{\rho\nu\alpha\beta_n} p^\alpha \\ & \left. + g_4 \gamma_5 \gamma_\mu \gamma^\rho (p_\rho g_{\nu\beta_n} - p_\nu g_{\rho\beta_n}) \right\} \\ & \times k_{\beta_1} \dots k_{\beta_{n-1}} (k^\mu \epsilon^\nu - k^\nu \epsilon^\mu) + \text{H.c.} \end{aligned} \quad (19)$$

The vertex factors can be simplified to

$$\Gamma_{\mu_1 \dots \mu_2}^{\text{had}} = \frac{1}{m_R^n} \tilde{\Gamma}_{\text{had}}^{\nu_1 \dots \nu_n} \tilde{O}_{(\nu_1 \dots \nu_n) \mu_1 \dots \mu_n}^{(n+1/2)}(p_R) \quad (20)$$

$$\Gamma_{\text{em}}^{\mu_1 \dots \mu_2} = \frac{1}{m_R^n} \tilde{O}_{(\nu_1 \dots \nu_n) \mu_1 \dots \mu_n}^{(n+1/2)}(p_R) \tilde{\Gamma}_{\nu_1 \dots \nu_n}^{\text{em}} \quad (21)$$

where $\tilde{O}_{(\nu_1 \dots \nu_n) \mu_1 \dots \mu_n}^{(n+1/2)}(p_R)$ is the interaction operator defined by

$$\begin{aligned} & \tilde{O}_{(\nu_1 \dots \nu_n) \mu_1 \dots \mu_n}^{(n+1/2)}(p_R) = \\ & O_{(\nu_1 \dots \nu_n, \alpha_1 \dots \alpha_n) \mu_1 \dots \mu_n}^{(n+1/2)}(p_R) \gamma^{\alpha_1} \dots \gamma^{\alpha_n}. \end{aligned} \quad (22)$$

In the present work we use the propagator

$$P_{\mu_1 \dots \mu_n; \nu_1 \dots \nu_n}(p_R) = \frac{\not{p}_R + m_R}{p_R^2 - m_R^2 + im_R \Gamma} \tilde{\mathcal{P}}_{\mu_1 \dots \mu_n; \nu_1 \dots \nu_n}^{n+1/2}(p_R), \quad (23)$$

where $\tilde{\mathcal{P}}_{\mu_1 \dots \mu_n; \nu_1 \dots \nu_n}^{n+1/2}(p_R)$ is the on-shell projection operator. The complicated form of the projection operator will be discussed later.

The production amplitude is obtained by sandwiching the propagator between the two vertices, i.e.,

$$\mathcal{M}_{\text{res}}^{n+1/2} = \bar{u}_\Lambda \Gamma_{\mu_1 \dots \mu_n}^{\text{had}} P_{(n+1/2)}^{\mu_1 \dots \mu_n, \nu_1 \dots \nu_n}(p_R) \Gamma_{\nu_1 \dots \nu_n}^{\text{em}} u_p. \quad (24)$$

By inserting Eqs. (20), (21), and (23) into Eq. (24) we obtain

$$\begin{aligned} \mathcal{M}_{\text{res}}^{n+1/2} = & \bar{u}_\Lambda \tilde{\Gamma}_{\text{had}}^{\alpha_1 \dots \alpha_n} \tilde{O}_{(\alpha_1 \dots \alpha_n) \mu_1 \dots \mu_n}^{n+1/2}(p_R) \\ & \times \frac{1}{m_R^{2n}} P_{(n+1/2)}^{\mu_1 \dots \mu_n, \nu_1 \dots \nu_n}(p_R) \\ & \times \tilde{O}_{n+1/2}^{(\beta_1 \dots \beta_n) \nu_1 \dots \nu_n}(p_R) \tilde{\Gamma}_{\text{em}}^{\beta_1 \dots \beta_n} u_p, \\ = & \bar{u}_\Lambda \tilde{\Gamma}_{\text{had}}^{\alpha_1 \dots \alpha_n} \tilde{O}_{(\alpha_1 \dots \alpha_n) \mu_1 \dots \mu_n}^{n+1/2}(p_R) \\ & \times \frac{1}{m_R^{2n}} \frac{\not{p}_R + m_R}{p_R^2 - m_R^2 + im_R \Gamma} \\ & \times \mathcal{P}_{(n+1/2)}^{\mu_1 \dots \mu_n, \nu_1 \dots \nu_n}(p_R) \tilde{O}_{n+1/2}^{(\beta_1 \dots \beta_n) \nu_1 \dots \nu_n}(p_R) \\ & \times \tilde{\Gamma}_{\text{em}}^{\beta_1 \dots \beta_n} u_p. \end{aligned} \quad (25)$$

The above formulation is simplified by considering the orthogonalities of the projection operator,

$$\begin{aligned} \gamma_{\mu_i} \mathcal{P}_{(n+1/2)}^{\mu_1 \dots \mu_n, \nu_1 \dots \nu_n}(p_R) &= \mathcal{P}_{(n+1/2)}^{\mu_1 \dots \mu_n, \nu_1 \dots \nu_n}(p_R) \gamma_{\nu_i} \\ &= 0, \end{aligned} \quad (26)$$

and

$$\begin{aligned} p_{R\mu_i} \mathcal{P}_{(n+1/2)}^{\mu_1 \dots \mu_n, \nu_1 \dots \nu_n}(p_R) &= p_{R\nu_i} \mathcal{P}_{(n+1/2)}^{\mu_1 \dots \mu_n, \nu_1 \dots \nu_n}(p_R) \\ &= 0, \end{aligned} \quad (27)$$

with $i = 1, 2, \dots, n$.

Thus, the scattering amplitude can be written as

$$\begin{aligned}
\mathcal{M}_{\text{res}}^{n+1/2} &= \bar{u}_\Lambda \prod_{i=1}^n \not{p}_R g_{\alpha_i \mu_i} \tilde{\Gamma}_{\text{had}}^{\alpha_1 \dots \alpha_n} \frac{1}{m_R^{2n}} \frac{\not{p}_R + m_R}{p_R^2 - m_R^2 + im_R \Gamma} \mathcal{P}_{(n+1/2)}^{\mu_1 \dots \mu_n, \nu_1 \dots \nu_n} (p_R) \prod_{i=1}^n \not{p}_R g_{\beta_j \nu_j} \tilde{\Gamma}_{\text{em}}^{\beta_1 \dots \beta_n} u_p \\
&= \bar{u}_\Lambda \tilde{\Gamma}_{\mu_1 \dots \mu_n}^{\text{had}} \frac{p_R^{2n}}{m_R^{2n}} \frac{\not{p}_R + m_R}{p_R^2 - m_R^2 + im_R \Gamma} \mathcal{P}_{(n+1/2)}^{\mu_1 \dots \mu_n, \nu_1 \dots \nu_n} (p_R) \tilde{\Gamma}_{\text{em}}^{\beta_1 \dots \beta_n} u_p.
\end{aligned} \tag{28}$$

The above equation shows how a consistent interaction structure constructed intuitively.

C. Propagators

The propagators used in this model are constructed from the corresponding particle projection operators. The generalized projection operator has been explored by Huang, *et al.* in Ref. [11]. The projection operator for spin-11/2 can be written as

$$\begin{aligned}
\mathcal{P}_{\mu_1 \mu_2 \mu_3 \mu_4}^{\nu_1 \nu_2 \nu_3 \nu_4, 11/2} &= \frac{1}{1440} \sum_{P(\mu), P(\nu)} \left\{ P_{\mu\nu} P_{\mu_1 \nu_1} P_{\mu_2 \nu_2} P_{\mu_3 \nu_3} P_{\mu_4 \nu_4} - \frac{10}{11} P_{\mu\mu_1} P_{\nu\nu_1} P_{\mu_2 \nu_2} P_{\mu_3 \nu_3} P_{\mu_4 \nu_4} \right. \\
&\quad + \frac{5}{33} P_{\mu\mu_1} P_{\nu\nu_1} P_{\mu_2 \mu_3} P_{\nu_2 \nu_3} P_{\mu_4 \nu_4} + \frac{5}{11} \gamma^\rho \gamma^\sigma P_{\mu\rho} P_{\nu\sigma} P_{\mu_1 \nu_1} P_{\mu_2 \nu_2} P_{\mu_3 \nu_3} P_{\mu_4 \nu_4} \\
&\quad \left. - \frac{10}{33} \gamma^\rho \gamma^\sigma P_{\mu\rho} P_{\nu\sigma} P_{\mu_1 \mu_2} P_{\nu_1 \nu_2} P_{\mu_3 \nu_3} P_{\mu_4 \nu_4} + \frac{5}{231} \gamma^\rho \gamma^\sigma P_{\mu\rho} P_{\nu\sigma} P_{\mu_1 \mu_2} P_{\nu_1 \nu_2} P_{\mu_3 \mu_4} P_{\nu_3 \nu_4} \right\}, \tag{29}
\end{aligned}$$

and for spin-13/2 particles the projection operator is

$$\begin{aligned}
\mathcal{P}_{\mu_1 \mu_2 \mu_3 \mu_4 \mu_5}^{\nu_1 \nu_2 \nu_3 \nu_4 \nu_5, 13/2} &= \frac{1}{(6!)^2} \sum_{P(\mu), P(\nu)} \left\{ P_{\mu\nu} P_{\mu_1 \nu_1} P_{\mu_2 \nu_2} P_{\mu_3 \nu_3} P_{\mu_4 \nu_4} P_{\mu_5 \nu_5} - \frac{15}{13} P_{\mu\mu_1} P_{\nu\nu_1} P_{\mu_2 \nu_2} P_{\mu_3 \nu_3} P_{\mu_4 \nu_4} P_{\mu_5 \nu_5} \right. \\
&\quad + \frac{45}{143} P_{\mu\mu_1} P_{\nu\nu_1} P_{\mu_2 \mu_3} P_{\nu_2 \nu_3} P_{\mu_4 \nu_4} P_{\mu_5 \nu_5} - \frac{5}{429} P_{\mu\mu_1} P_{\nu\nu_1} P_{\mu_2 \mu_3} P_{\nu_2 \nu_3} P_{\mu_4 \mu_5} P_{\nu_4 \nu_5} \\
&\quad + \frac{6}{13} \gamma^\rho \gamma^\sigma P_{\mu\rho} P_{\nu\sigma} P_{\mu_1 \nu_1} P_{\mu_2 \nu_2} P_{\mu_3 \nu_3} P_{\mu_4 \nu_4} P_{\mu_5 \nu_5} - \frac{60}{143} \gamma^\rho \gamma^\sigma P_{\mu\rho} P_{\nu\sigma} P_{\mu_1 \mu_2} P_{\nu_1 \nu_2} P_{\mu_3 \nu_3} P_{\mu_4 \nu_4} P_{\mu_5 \nu_5} \\
&\quad \left. + \frac{30}{429} \gamma^\rho \gamma^\sigma P_{\mu\rho} P_{\nu\sigma} P_{\mu_1 \mu_2} P_{\nu_1 \nu_2} P_{\mu_3 \mu_4} P_{\nu_3 \nu_4} P_{\mu_5 \nu_5} \right\}, \tag{30}
\end{aligned}$$

while the projection operator for spin-15/2 particles reads

$$\begin{aligned}
\mathcal{P}_{\mu_1 \mu_2 \mu_3 \mu_4 \mu_5 \mu_6}^{\nu_1 \nu_2 \nu_3 \nu_4 \nu_5 \nu_6, 15/2} &= \frac{1}{(7!)^2} \sum_{P(\mu), P(\nu)} \left\{ P_{\mu\nu} P_{\mu_1 \nu_1} P_{\mu_2 \nu_2} P_{\mu_3 \nu_3} P_{\mu_4 \nu_4} P_{\mu_5 \nu_5} P_{\mu_6 \nu_6} \right. \\
&\quad - \frac{21}{15} P_{\mu\mu_1} P_{\nu\nu_1} P_{\mu_2 \nu_2} P_{\mu_3 \nu_3} P_{\mu_4 \nu_4} P_{\mu_5 \nu_5} P_{\mu_6 \nu_6} + \frac{7}{13} P_{\mu\mu_1} P_{\nu\nu_1} P_{\mu_2 \mu_3} P_{\nu_2 \nu_3} P_{\mu_4 \nu_4} P_{\mu_5 \nu_5} P_{\mu_6 \nu_6} \\
&\quad - \frac{7}{143} P_{\mu\mu_1} P_{\nu\nu_1} P_{\mu_2 \mu_3} P_{\nu_2 \nu_3} P_{\mu_4 \mu_5} P_{\nu_4 \nu_5} P_{\mu_6 \nu_6} + \frac{7}{15} \gamma^\rho \gamma^\sigma P_{\mu\rho} P_{\nu\sigma} P_{\mu_1 \nu_1} P_{\mu_2 \nu_2} P_{\mu_3 \nu_3} P_{\mu_4 \nu_4} P_{\mu_5 \nu_5} P_{\mu_6 \nu_6} \\
&\quad - \frac{7}{13} \gamma^\rho \gamma^\sigma P_{\mu\rho} P_{\nu\sigma} P_{\mu_1 \mu_2} P_{\nu_1 \nu_2} P_{\mu_3 \nu_3} P_{\mu_4 \nu_4} P_{\mu_5 \nu_5} P_{\mu_6 \nu_6} + \frac{21}{143} \gamma^\rho \gamma^\sigma P_{\mu\rho} P_{\nu\sigma} P_{\mu_1 \mu_2} P_{\nu_1 \nu_2} P_{\mu_3 \mu_4} P_{\nu_3 \nu_4} P_{\mu_5 \nu_5} P_{\mu_6 \nu_6} \\
&\quad \left. - \frac{7}{1287} \gamma^\rho \gamma^\sigma P_{\mu\rho} P_{\nu\sigma} P_{\mu_1 \mu_2} P_{\nu_1 \nu_2} P_{\mu_3 \mu_4} P_{\nu_3 \nu_4} P_{\mu_5 \mu_6} P_{\nu_5 \nu_6} \right\}, \tag{31}
\end{aligned}$$

The projection operators written above fulfill the orthogonality condition given by Eq.(26). According to Eq.(28), the propagator for spin-11/2 resonance can be written as

$$\mathcal{P}_{\mu_1 \mu_2 \mu_3 \mu_4}^{\nu_1 \nu_2 \nu_3 \nu_4, 11/2} = \frac{s^5}{m_R^{10}} \frac{(\not{p} + \not{k} + m_R)}{(s - m_R^2 + im_R \Gamma_R)} \mathcal{P}_{\mu_1 \mu_2 \mu_3 \mu_4}^{\nu_1 \nu_2 \nu_3 \nu_4, 11/2}, \tag{32}$$

whereas for spin-13/2 and spin-15/2 resonances the propagators read

$$\mathcal{P}_{\mu_1 \mu_2 \mu_3 \mu_4 \mu_5}^{\nu_1 \nu_2 \nu_3 \nu_4 \nu_5, 13/2} = \frac{s^6}{m_R^{12}} \frac{(\not{p} + \not{k} + m_R)}{(s - m_R^2 + im_R \Gamma_R)} \mathcal{P}_{\mu_1 \mu_2 \mu_3 \mu_4 \mu_5}^{\nu_1 \nu_2 \nu_3 \nu_4 \nu_5, 13/2} \tag{33}$$

and

$$\mathcal{P}_{\mu_1 \mu_2 \mu_3 \mu_4 \mu_5 \mu_6}^{\nu_1 \nu_2 \nu_3 \nu_4 \nu_5 \nu_6, 15/2} = \frac{s^7}{m_R^{14}} \frac{(\not{p} + \not{k} + m_R)}{(s - m_R^2 + im_R \Gamma_R)} \mathcal{P}_{\mu_1 \mu_2 \mu_3 \mu_4 \mu_5 \mu_6}^{\nu_1 \nu_2 \nu_3 \nu_4 \nu_5 \nu_6, 15/2}, \tag{34}$$

respectively, with $s = p_R^2 = (p + k)^2 = W^2$. Notice that the factors s^5/m_R^{10} , s^6/m_R^{12} and s^7/m_R^{14} originate from the consequence of the consistent interaction.

D. Hadronic and Electromagnetic Vertices

By using the above prescription we obtain that the hadronic and electromagnetic vertices for spin-11/2 reads as

$$\Gamma_{\text{had}}^{\mu\mu_1\mu_2\mu_3\mu_4\pm} = \frac{g_{KYR}}{m_R^6} \Gamma_{\mp} [(p_{\Lambda} \cdot q - \not{p}_{\Lambda} \not{q}) \gamma^{\mu} + \not{p}_{\Lambda} q^{\mu} - \not{q} p_{\Lambda}^{\mu}] p_{\Lambda}^{\mu_1} p_{\Lambda}^{\mu_2} p_{\Lambda}^{\mu_3} p_{\Lambda}^{\mu_4} \quad (35)$$

and

$$\begin{aligned} \Gamma_{\text{em}}^{\nu\nu_1\nu_2\nu_3\nu_4\pm} &= \frac{-i}{m_R^6} \left[g_1 p^{\nu} (\not{k} \not{\epsilon} - \not{\epsilon} \not{k}) + g_2 (k^{\nu} p \cdot \epsilon - \epsilon^{\nu} p \cdot k) + g_3 (\epsilon^{\nu} \not{k} - k^{\nu} \not{\epsilon}) \not{p} + g_4 \gamma^{\nu} (\not{k} \not{\epsilon} - \not{\epsilon} \not{k}) \not{p} \right. \\ &\quad \left. + g_5 \gamma^{\nu} (p \cdot \epsilon \not{k} - p \cdot k \not{\epsilon}) \right] k^{\nu_1} k^{\nu_2} k^{\nu_3} k^{\nu_4} \Gamma_{\pm}, \end{aligned} \quad (36)$$

respectively, whereas for the spin-13/2 resonance

$$\Gamma_{\text{had}}^{\mu\mu_1\mu_2\mu_3\mu_4\mu_5\pm} = \frac{g_{KYR}}{m_R^7} \Gamma_{\pm} [(p_{\Lambda} \cdot q - \not{p}_{\Lambda} \not{q}) \gamma^{\mu} + \not{p}_{\Lambda} q^{\mu} - \not{q} p_{\Lambda}^{\mu}] p_{\Lambda}^{\mu_1} p_{\Lambda}^{\mu_2} p_{\Lambda}^{\mu_3} p_{\Lambda}^{\mu_4} p_{\Lambda}^{\mu_5}, \quad (37)$$

and

$$\begin{aligned} \Gamma_{\text{em}}^{\nu\nu_1\nu_2\nu_3\nu_4\nu_5\pm} &= \frac{-i}{m_R^7} \left[g_1 p^{\nu} (\not{k} \not{\epsilon} - \not{\epsilon} \not{k}) + g_2 (k^{\nu} p \cdot \epsilon - \epsilon^{\nu} p \cdot k) + g_3 (\epsilon^{\nu} \not{k} - k^{\nu} \not{\epsilon}) \not{p} + g_4 \gamma^{\nu} (\not{k} \not{\epsilon} - \not{\epsilon} \not{k}) \not{p} \right. \\ &\quad \left. + g_5 \gamma^{\nu} (p \cdot \epsilon \not{k} - p \cdot k \not{\epsilon}) \right] k^{\nu_1} k^{\nu_2} k^{\nu_3} k^{\nu_4} k^{\nu_5} \Gamma_{\mp}, \end{aligned} \quad (38)$$

respectively. The above result indicates that the number of momentum dependence increases with the number of spin. This conclusion was previously made by Ref. [11].

For the spin-15/2 resonance the hadronic and electromagnetic vertices are given by

$$\Gamma_{\text{had}}^{\mu\mu_1\mu_2\mu_3\mu_4\mu_5\mu_6\pm} = \frac{g_{KYR}}{m_R^8} \Gamma_{\pm} [(p_{\Lambda} \cdot q - \not{p}_{\Lambda} \not{q}) \gamma^{\mu} + \not{p}_{\Lambda} q^{\mu} - \not{q} p_{\Lambda}^{\mu}] p_{\Lambda}^{\mu_1} p_{\Lambda}^{\mu_2} p_{\Lambda}^{\mu_3} p_{\Lambda}^{\mu_4} p_{\Lambda}^{\mu_5} p_{\Lambda}^{\mu_6}, \quad (39)$$

and

$$\begin{aligned} \Gamma_{\text{em}}^{\nu\nu_1\nu_2\nu_3\nu_4\nu_5\nu_6\pm} &= \frac{-i}{m_R^8} \left[g_1 p^{\nu} (\not{k} \not{\epsilon} - \not{\epsilon} \not{k}) + g_2 (k^{\nu} p \cdot \epsilon - \epsilon^{\nu} p \cdot k) + g_3 (\epsilon^{\nu} \not{k} - k^{\nu} \not{\epsilon}) \not{p} + g_4 \gamma^{\nu} (\not{k} \not{\epsilon} - \not{\epsilon} \not{k}) \not{p} \right. \\ &\quad \left. + g_5 \gamma^{\nu} (p \cdot \epsilon \not{k} - p \cdot k \not{\epsilon}) \right] k^{\nu_1} k^{\nu_2} k^{\nu_3} k^{\nu_4} k^{\nu_5} k^{\nu_6} \Gamma_{\mp}, \end{aligned} \quad (40)$$

respectively. The above formalism is valid for both positive and negative parities, for which the parity factors are denoted by $\Gamma_{+} = i\gamma_5$ and $\Gamma_{-} = 1$, respectively.

E. Production Amplitudes

As stated above the production amplitudes for spin-11/2, -13/2, and -15/2 resonances are obtained by sandwiching the propagators given by Eqs. (32), (33), and (34) between the corresponding hadronic vertex factors given by Eqs. (35), (37), and (39), and electromagnetic vertex factors given by Eqs. (36), (38), and (40), respectively. As a result we obtain the amplitude for spin-11/2

$$\begin{aligned} \mathcal{M}_{11/2}^{\pm} &= \bar{u}_{\Lambda} \gamma_5 \{-s \pm m_R (\not{p} + \not{k})\} \left[7(33c_1^4 + 18c_1^2 c_2 c_3 + 7c_2^2 c_3^2) \times \{-p_{\Lambda\nu} + \frac{1}{s} c_{\Lambda} (p+k)_{\nu}\} - 14c_1 c_2 (6c_1^2 + 2c_2 c_3) \right. \\ &\quad \times \{-k_{\nu} + \frac{1}{s} c_k (p+k)_{\nu}\} + (21c_1^4 + 14c_1^2 c_2 c_3 + c_2^2 c_3^2) \{-\not{p}_{\Lambda} + \frac{1}{s} c_{\Lambda} (\not{p} + \not{k})\} \{-\gamma_{\nu} + \frac{1}{s} (\not{p} + \not{k})(p+k)_{\nu}\} \\ &\quad - 14c_1 (6c_1^2 + 2c_2 c_3) \{-\not{p}_{\Lambda} + \frac{1}{s} c_{\Lambda} (\not{p} + \not{k})\} \{-\not{k} + \frac{1}{s} c_k (\not{p} + \not{k})\} \{-p_{\Lambda\nu} + \frac{1}{s} c_{\Lambda} (p+k)_{\nu}\} + 4c_2 (7c_1^2 + c_2 c_3) \\ &\quad \times \{-\not{p}_{\Lambda} + \frac{1}{s} c_{\Lambda} (\not{p} + \not{k})\} \{-\not{k} + \frac{1}{s} c_k (\not{p} + \not{k})\} \{-k_{\nu} + \frac{1}{s} c_k (p+k)_{\nu}\} \left. \right] \\ &\quad \times \left[G_{1a} p^{\nu} (\not{k} \not{\epsilon} - \not{\epsilon} \not{k}) + G_{2a} (k^{\nu} p \cdot \epsilon - \epsilon^{\nu} p \cdot k) + G_{3a} (\epsilon^{\nu} \not{k} - k^{\nu} \not{\epsilon}) \not{p} \right] u_p, \end{aligned} \quad (41)$$

with:

$$G_{1a} = \frac{s^5 g_{KYRg1}}{231m_R^{22}(s - m_R^2 + im_R\Gamma_R)}, \quad (42)$$

$$G_{2a} = \frac{s^5 g_{KYRg2}}{231m_R^{22}(s - m_R^2 + im_R\Gamma_R)}, \quad (43)$$

$$G_{3a} = \frac{s^5 g_{KYRg3}}{231m_R^{22}(s - m_R^2 + im_R\Gamma_R)}. \quad (44)$$

The production amplitude for spin-13/2 particle is given by

$$\begin{aligned} \mathcal{M}_{13/2}^\pm &= \bar{u}_\Lambda \gamma_5 \{s \pm m_R(\not{p} + \not{k})\} \left[3c_1(143c_1^4 + 110c_1^2c_2c_3 + 15c_2^2c_3^2) \left\{ -p_{\Lambda\nu} + \frac{1}{s}c_\Lambda(p+k)_\nu \right\} - 5c_2(33c_1^4 \right. \\ &\quad + 18c_1^2c_2c_3 + c_2^2c_3^2) \left\{ -k_\nu + \frac{1}{s}c_k(p+k)_\nu \right\} + c_1(33c_1^4 + 120c_1^2c_2c_3 + 5c_2^2c_3^2) \left\{ -\not{p}_\Lambda + \frac{1}{s}c_\Lambda(\not{p} + \not{k}) \right\} \\ &\quad \times \left\{ -\gamma_\nu + \frac{1}{s}(\not{p} + \not{k})(p+k)_\nu \right\} - 5(33c_1^4 + 18c_1^2c_2c_3 + c_2^2c_3^2) \left\{ -\not{p}_\Lambda + \frac{1}{s}c_\Lambda(\not{p} + \not{k}) \right\} \left\{ -\not{k} + \frac{1}{s}c_k(\not{p} + \not{k}) \right\} \\ &\quad \times \left\{ -p_{\Lambda\nu} + \frac{1}{s}c_\Lambda(p+k)_\nu \right\} + 20c_1c_2(3c_1^2 + c_2c_3) \left\{ -\not{p}_\Lambda + \frac{1}{s}c_\Lambda(\not{p} + \not{k}) \right\} \left\{ -\not{k} + \frac{1}{s}c_k(\not{p} + \not{k}) \right\} \\ &\quad \times \left\{ -k_\nu + \frac{1}{s}c_k(p+k)_\nu \right\} \left. \right] \left[G_{1b}p^\nu(\not{k}\not{\epsilon} - \not{\epsilon}\not{k}) + G_{2b}(k^\nu p \cdot \epsilon - \epsilon^\nu p \cdot k) + G_{3b}(\epsilon^\nu \not{k} - k^\nu \not{\epsilon})\not{p} \right] u_p, \quad (45) \end{aligned}$$

with

$$G_{1b} = \frac{s^6 g_{KYRg1}}{429m_R^{26}(s - m_R^2 + im_R\Gamma_R)}, \quad (46)$$

$$G_{2b} = \frac{s^6 g_{KYRg2}}{429m_R^{26}(s - m_R^2 + im_R\Gamma_R)}, \quad (47)$$

$$G_{3b} = \frac{s^6 g_{KYRg3}}{429m_R^{26}(s - m_R^2 + im_R\Gamma_R)}. \quad (48)$$

Finally, the amplitude for spin-15/2 resonance reads

$$\begin{aligned} \mathcal{M}_{15/2}^\pm &= \bar{u}_\Lambda \gamma_5 \{-s \pm m_R(\not{p} + \not{k})\} \left[45(143c_1^6 + 143c_1^4c_2c_3 + 33c_1^2c_2^2c_3^2 + c_2^3c_3^3) \left\{ -p_{\Lambda\nu} + \frac{1}{s}c_\Lambda(p+k)_\nu \right\} \right. \\ &\quad - 9c_1c_2(286c_1^4 + 220c_1^2c_2c_3 + 30c_2^2c_3^2) \left\{ -k_\nu + \frac{1}{s}c_k(p+k)_\nu \right\} + (429c_1^6 + 495c_1^4c_2c_3 + 135c_1^2c_2^2c_3^2) \\ &\quad \times \left\{ -\not{p}_\Lambda + \frac{1}{s}c_\Lambda(\not{p} + \not{k}) \right\} \left\{ -\gamma_\nu + \frac{1}{s}(\not{p} + \not{k})(p+k)_\nu \right\} - 18c_1(143c_1^4 + 110c_1c_2c_3 + 15c_2^2c_3^2) \\ &\quad \times \left\{ -\not{p}_\Lambda + \frac{1}{s}c_\Lambda(\not{p} + \not{k}) \right\} \left\{ -\not{k} + \frac{1}{s}c_k(\not{p} + \not{k}) \right\} \left\{ -p_{\Lambda\nu} + \frac{1}{s}c_\Lambda(p+k)_\nu \right\} + 30c_2(33c_1^4 + 18c_1c_2c_3^2 + c_2^2c_3^2) \\ &\quad \times \left\{ -\not{p}_\Lambda + \frac{1}{s}c_\Lambda(\not{p} + \not{k}) \right\} \left\{ -\not{k} + \frac{1}{s}c_k(\not{p} + \not{k}) \right\} \left\{ -k_\nu + \frac{1}{s}c_k(p+k)_\nu \right\} \left. \right] \\ &\quad \times \left[G_{1c}p^\nu(\not{k}\not{\epsilon} - \not{\epsilon}\not{k}) + G_{2c}(k^\nu p \cdot \epsilon - \epsilon^\nu p \cdot k) + G_{3c}(\epsilon^\nu \not{k} - k^\nu \not{\epsilon})\not{p} \right] u_p, \quad (49) \end{aligned}$$

with

$$G_{1c} = \frac{s^7 g_{KYRg1}}{6435m_R^{30}(s - m_R^2 + im_R\Gamma_R)}, \quad (50)$$

$$G_{2c} = \frac{s^7 g_{KYRg2}}{6435m_R^{30}(s - m_R^2 + im_R\Gamma_R)}, \quad (51)$$

$$G_{3c} = \frac{s^7 g_{KYRg3}}{6435m_R^{30}(s - m_R^2 + im_R\Gamma_R)}. \quad (52)$$

Note that in the fitting process only the product of the hadronic and electromagnetic couplings, i.e., g_{KYRg_i} with $i = 1, 2, 3$, are extracted from the data. Furthermore, in the production amplitudes given by Eqs. (41),

(45), and (49) we have used the following definitions,

$$c_1 = b_\Lambda - c_\Lambda c_k/s, \quad (53a)$$

$$c_2 = m_\Lambda^2 - c_\Lambda^2/s, \quad (53b)$$

$$c_3 = c_k^2/s - k^2, \quad (53c)$$

$$c_4 = 2b_p + k^2, \quad (53d)$$

$$c_5 = 4b_p + k^2, \quad (53e)$$

$$b_p = p \cdot k, \quad (53f)$$

$$b_\Lambda = p_\Lambda \cdot k, \quad (53g)$$

$$b_q = q \cdot k, \quad (53h)$$

$$c_p = (p + k) \cdot p, \quad (53i)$$

$$c_\Lambda = (p + k) \cdot p_\Lambda, \quad (53j)$$

$$c_k = (p + k) \cdot k, \quad (53k)$$

$$c_s = 1 - c_\Lambda/s. \quad (53l)$$

F. Calculation of the observables

The production amplitudes given by Eqs. (41), (45), and (49) can be decomposed into six gauge and Lorentz invariant matrices M_i through

$$\mathcal{M}_{fi} = \bar{u}_\Lambda \sum_{i=1}^6 A_i M_i u_p, \quad (54)$$

where the gauge and Lorentz invariant matrices M_i are given by [12, 13]:

$$M_1 = \gamma_5 \not{k}, \quad (55)$$

$$M_2 = 2\gamma_5 (q \cdot \epsilon P \cdot k - q \cdot k P \cdot \epsilon), \quad (56)$$

$$M_3 = \gamma_5 (q \cdot k \not{\epsilon} - q \cdot \epsilon \not{k}), \quad (57)$$

$$M_4 = i\varepsilon_{\mu\nu\rho\sigma} \gamma^\mu q^\nu \epsilon^\rho k^\sigma, \quad (58)$$

$$M_5 = \gamma_5 (q \cdot \epsilon k^2 - q \cdot k k \cdot \epsilon), \quad (59)$$

$$M_6 = \gamma_5 (k \cdot \epsilon \not{k} - k^2 \not{\epsilon}), \quad (60)$$

where $P = \frac{1}{2}(p + p_\Lambda)$ and $\varepsilon_{\mu\nu\rho\sigma}$ is the Levi-Civita antisymmetric tensor. All observables required for fitting the experimental data can be calculated from the form function A_i extracted from Eq. (54), after adding the contributions from all involved intermediate states. The form functions A_i for baryon resonances with spins up to 9/2 are given in the previous works [1, 14], whereas those with spins 11/2, 13/2, and 15/2 considered in the present work are given in Appendix A.

G. Pole Position

Besides the Breit-Wigner parameters, such as mass, width, and branching ratios, the Particle Data Group has recently listed new information on the resonance properties, i.e., the pole position. It is obvious that the Breit-Wigner parameters extracted in each model depend highly on the background terms of the model. Therefore,

all resonance properties obtained by using such parameterization is difficult to compare with those obtained from other models. This problem does not appear in the case of pole position. Currently, the pole position has been extensively used in the realm of hadronic physics. In the Particle Data Book 2018 the pole positions of resonance are listed before the Breit-Wigner parameters. The placement shows that the pole positions is currently considered as the important properties of a resonance.

In principle, the pole position can be calculated by setting the denominator of the scattering amplitude to zero. Approaching the pole position the scattering amplitude of a resonance increases dramatically. Since the resonance scattering amplitude becomes extremely larger than contributions from other intermediate states, the resonance property calculated at the pole position is insensitive to the contribution of background terms. As a result, the evaluation of resonance properties at the pole position is practically model independent.

In the present work, the pole position properties of a resonance are the resonance mass and width. They are defined *via*

$$\sqrt{s_R} = M_{\text{pole}} - i\Gamma_{\text{pole}}/2. \quad (61)$$

As previously stated, this is obtained by setting the denominator of scattering amplitude to zero, i.e.,

$$s_R - m_R^2 + im_R\Gamma(s_R) = 0. \quad (62)$$

Notice that the above equation cannot be directly calculated, since in the present study we use $\Gamma(s)$ that depends on the total c.m. energy. Therefore, the solution of Eq. (62) must be obtained numerically.

III. RESULTS AND DISCUSSION

In the present work, the isobar model used to analyze the effect of spin-11/2 and -13/2 nucleon resonances in the $K\Lambda$ channels is based on our previous model developed to describe all available data in these channels [3]. Furthermore, in this study we also investigate the effect of spin-11/2, -13/2, and -15/2 Δ resonances in the $K\Sigma$ reaction channels. Along with the nucleon resonances used in the $K\Lambda$ channels, these Δ resonances are listed in Table I. In total, there are 23 nucleon resonances included in our analysis for the $K\Lambda$ and $K\Sigma$ channels and, in addition, 17 Δ resonances in the $K\Sigma$ channels with spins up to spin-15/2. The result obtained in all channels will be discussed in the following subsections.

A. $K\Lambda$ Channel

In Table III we present the leading coupling constants and other background parameters obtained from the previous work (Model B) [3] and current analysis (Model A). Note that in the present work we have omitted the

TABLE III: Coupling constants and other driving parameters of the background terms for $K\Lambda$ channels obtained in the present work (Model A) and the previous one (Model B) [3]. Error bars were not reported in Model B. See Ref. [3] for the explanation of the parameter notation.

Parameter	Model A	Model B
$g_{K\Lambda N}/\sqrt{4\pi}$	-4.40 ± 0.03	-3.00
$g_{K\Sigma N}/\sqrt{4\pi}$	0.90 ± 0.04	1.30
$G_{K^*}^V/4\pi$	0.08 ± 0.00	0.13
$G_{K^*}^T/4\pi$	-0.07 ± 0.00	0.17
$G_{K_1}^V/4\pi$	0.12 ± 0.00	0.13
$G_{K_1}^T/4\pi$	2.43 ± 0.00	3.89
$r_{K_1 K\gamma}$	0.52 ± 0.01	0.65
Λ_B (GeV)	0.89 ± 0.00	0.70
Λ_R (GeV)	1.09 ± 0.00	1.10
θ_{had} (deg)	94.31 ± 0.64	90.0
ϕ_{had} (deg)	90.00 ± 4.09	0.0
χ^2	13316	13867
N_{par}	264	247
N_{data}	9364	9364
χ^2/N_{dof}	1.46	1.52

$K^0\Lambda$ photoproduction data obtained from MAMI collaboration [15] due to the problem of data discrepancy as discussed in Ref. [3]. Furthermore, it was shown that by excluding these data from the database leads to a better model that can nicely reproduce the $\gamma n \rightarrow K^0\Lambda$ helicity asymmetry E [3]. It is important to note that Model B was also obtained from fitting without these data.

From Table III we can conclude that there is no dramatic changes in the background parameters after including the spin-11/2 and -13/2 nucleon resonances in the model. Nevertheless, the increase of $g_{K\Lambda N}$ coupling and the Born hadronic cutoff Λ_B shows that the inclusion of the two resonances increases the contribution of the background terms. We note that in the case of Kaon-Maid, the Born cutoff is very soft, i.e., $\Lambda_B = 0.637$ GeV [17]. Clearly, the Kaon-Maid model is dominated by the resonance terms, whereas the Born terms are strongly suppressed. Such situation is completely different from the case of pion or eta photoproduction and could raise a question, whether Kaon-Maid is a realistic phenomenological model.

The listed χ^2 values indicate that the agreement between model calculation and experimental data is significantly improved after including the two nucleon resonances, as clearly expected. Since the calculation includes two isospin channels, i.e., $\gamma p \rightarrow K^+\Lambda$ and $\gamma n \rightarrow K^0\Lambda$, in the followings we present comparison between model calculations and experimental data in details.

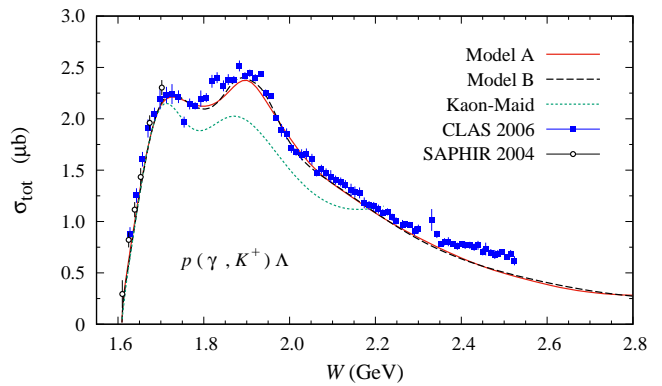


FIG. 2: Calculated total cross section of the $\gamma p \rightarrow K^+\Lambda$ channel obtained from previous [3] and present works, compared with the experimental data from the CLAS collaboration (solid squares [16]).

1. $K^+\Lambda$ Channel

Comparison between calculated $\gamma p \rightarrow K^+\Lambda$ total cross sections from Models A and B, Kaon-Maid, and experimental data is displayed in Fig. 2. Note that the experimental data shown in this figure are only for visual comparison. The data were not included in the fitting process, since differential and total cross sections data come from the same experiment.

Compared to the prediction of Kaon-Maid, both models A and B displayed in Fig. 2 show substantial improvement. However, since our main motivation in this work is to investigate the effect of spin-11/2 and 13/2 nucleon resonance, we will not compare our result with the prediction of Kaon-Maid in the following discussion, except in the case of total cross section, in which recent experimental data are in good agreement with Kaon-Maid for certain isospin channel. Both current and previous models seem to have a great agreement, with a tiny difference only at higher energy region, i.e., $W \geq 2.6$ GeV. The difference originates from the use of the high spin nucleon resonances, as obviously seen from their masses. However, since there are no available data in this energy region, no conclusion can be drawn at this point. Future experiments with 12 GeV electron source at JLab could be expected to reveal more information in this energy regime.

Both peaks shown by the two models seem to agree with each other, with minuscule difference at $W \approx 1.85$ GeV, where the second peak is attributed to the $P_{13}(1990)$ state, as discussed in Ref. [18].

More information can be obtained from the differential cross sections shown in Figs. 3 and 4. Figure 3 shows that the difference in the total cross sections of models A and B originate from the forward and backward regions of the differential cross section. Furthermore, as shown in Fig. 3 at backward angle ($\cos \theta = -0.70$), it is also apparent that the result of model A has a better agree-

ment than model B, except in the higher energy region, $W > 2.4$ GeV. Another interesting result is that the second peak of Model A is slightly shorter, but wider, than that of Model B. As a result, Model A yields a more accurate explanation of experimental data, especially for the CLAS 2010 [20] and Crystal Ball [21] ones. However, in the forward region Model A yields fewer peaks than Model B. Nevertheless, Model A seems to produce more natural shape of the cross section at the very forward angle, $\cos\theta = 0.90$, where unfortunately, the available experimental data from different collaborations produce uncertainty in differential cross section up to nearly 40%.

The angular distribution of differential cross section displayed in Fig. 4 shows that both models are in good agreement with experimental data. Furthermore, experimental data in higher energy region are better reproduced. This figure again shows that the inclusion of the high-spin resonances with higher masses does not influence the the cross section behavior in the lower energy region, where experimental data exist.

Figure 5 shows the single- and double-polarization observables, for which experimental data are abundantly available at present. In this case we do not see a dra-

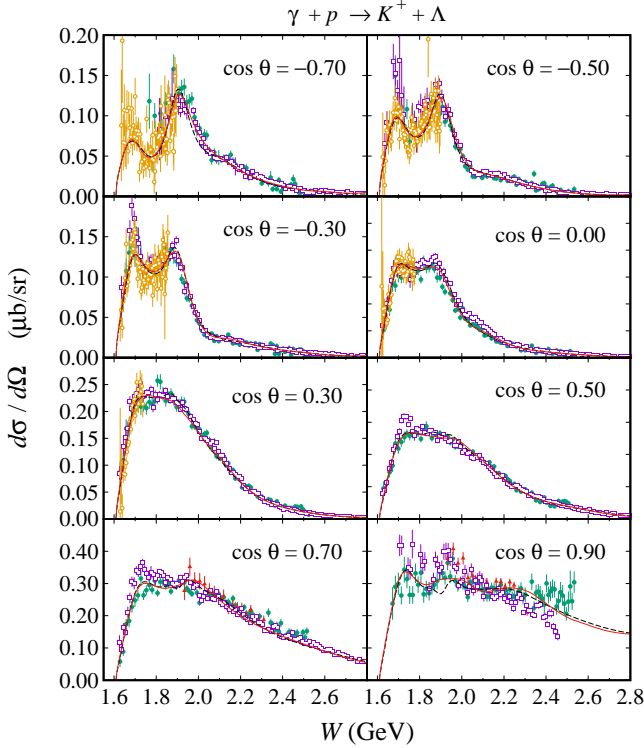


FIG. 3: Energy distributions of the $\gamma p \rightarrow K^+ \Lambda$ differential cross section obtained from Model A (solid red curves) and Model B (dashed black curves) for different values of $\cos\theta$. Experimental data shown in this figure are obtained from the LEPs 2006 (solid triangles [19]), CLAS 2006 (solid squares [16]), CLAS 2010 (solid circles [20]), and Crystal Ball 2014 (open circles [21]) collaborations.

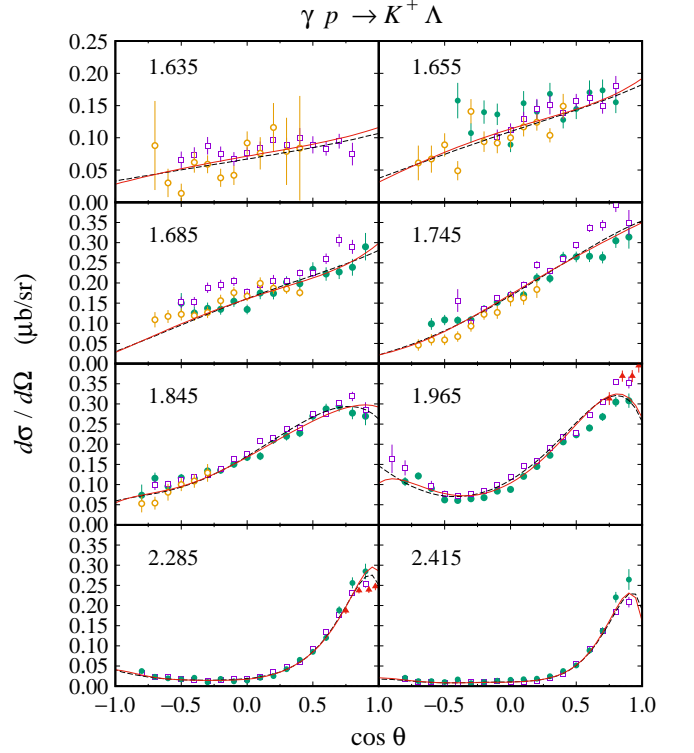


FIG. 4: As in Fig. 3, but for angular distribution. The corresponding value of total c.m. energy W in GeV is shown in each panel.

matic changes after including the spin-11/2 and 13/2 nucleon resonance in the model, except improvement in the agreement between model calculation and experimental data at forward direction and high energy region, which is expected due to the higher masses of these resonances. Nevertheless, we still see significant improvement in the beam-recoil double-polarization observables C_x and C_z at higher energies, where experimental data have large error bars. Note that only a small part of experimental data can be displayed in Fig. 5. More data are available in the fitting database, especially for the recoil polarization P , and are not shown in the figure due to their different kinematics.

2. $K^0 \Lambda$ Channel

The available data for the $K^0 \Lambda$ channel are significantly fewer than the $K^+ \Lambda$ one, given that the experiment with neutron target is more difficult to perform. The number of data included in this study is less than 1000, which will affect the accuracy between model calculation and experimental data. The calculation of this channel is performed by using the isospin relation of the hadronic coupling constants, as well as information on the neutral kaon transition moment and neutron helicity photon coupling obtained from PDG [4], in the $K^+ \Lambda$

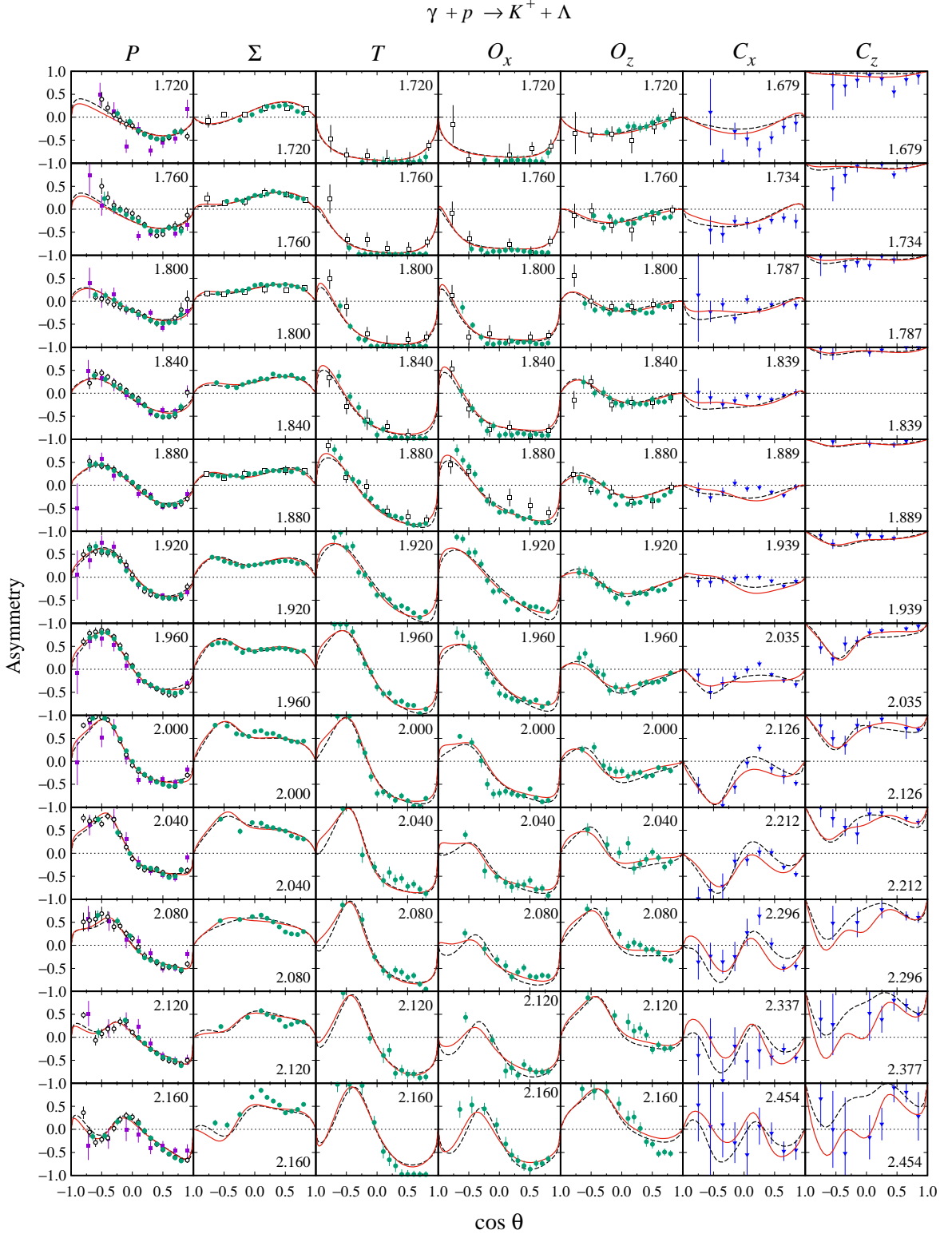


FIG. 5: Asymmetry of the single-polarization (P , Σ , and T), and double-polarization (O_x , O_z , C_x and C_z) observables for the $\gamma p \rightarrow K^+ \Lambda$ channel as a function of kaon angle for different total c.m. energies W shown in each panel. Dashed black curves are obtained from the previous isobar model [3], solid red curves are obtained from the present calculation. Experimental data shown in this figure are taken from the GRAAL 2009 (open squares [25]), CLAS 2006 (solid squares [16]), CLAS 2007 (solid triangles [26]), CLAS 2010 (open circles [20]), and CLAS 2016 (solid circles [27]) collaborations.

model as discussed in Refs. [22, 23]. Thus, investigation of the $K^0\Lambda$ channel can be considered as a direct test of isospin symmetry in kaon photoproduction.

Experimental data of this channel are already available from the CLAS g10 and g13 collaboration [24] and MAMI 2018 collaboration [15]. In the previous work [3], both data sets were included in the analysis. However, in the present work we exclude the data from the MAMI 2018 collaboration, since it was found that the data are more difficult to fit and have a discrepancy problem with the CLAS g10 and g13 data. Furthermore, in the present work our main motivation is to investigate the effect of the higher spin nucleon resonances, in which we need an accurate isobar model.

Figure 6 shows the calculated total cross section of the $\gamma n \rightarrow K^0\Lambda$ channel. Obviously, both models A and B yield similar cross section trend, except in the lower energy region and especially near the production threshold, where the cross section obtained from model B is steeper than that of the present work. All models give the total cross sections within the experimental error bars. As discussed in Ref. [23], threshold behavior of $K^0\Lambda$ photoproduction provides important information that can shed more light on the difference between pseudovector and pseudoscalar theories in the kaon photoproduction process. The absence of K^0 exchange in this channel also reduces the number of unknown parameters in the model. As a consequence, threshold properties of the $K^0\Lambda$ can be more accurately investigated. Note also that the over prediction of Kaon-Maid model is understandable, since it is pure prediction and the model was fitted to old data.

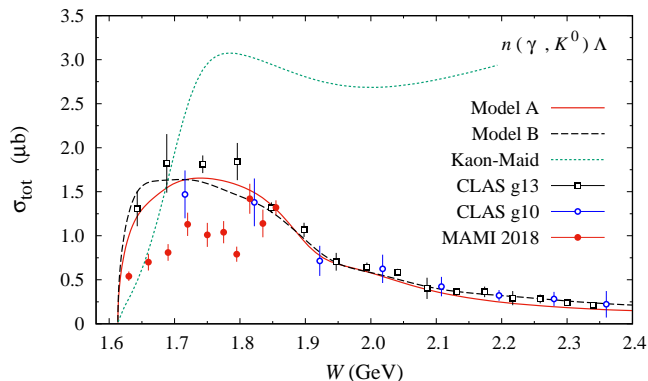


FIG. 6: Total cross section of the $\gamma n \rightarrow K^0\Lambda$ isospin channel calculated from different models. Experimental data are obtained from the CLAS g10 and g13 collaboration (open circles and open squares) [24] and MAMI 2018 collaboration (solid circles) [15]. Note that the data shown in this figure were not used in the fitting process and shown here only for comparison.

Figure 7 shows the differential cross section of the $\gamma n \rightarrow K^0\Lambda$ channel. At a glance, both models seem to be similar, especially at $W > 1.8$ GeV region. However, the inclusion of the two high-spin nucleon resonances leads to different differential cross section near the threshold.

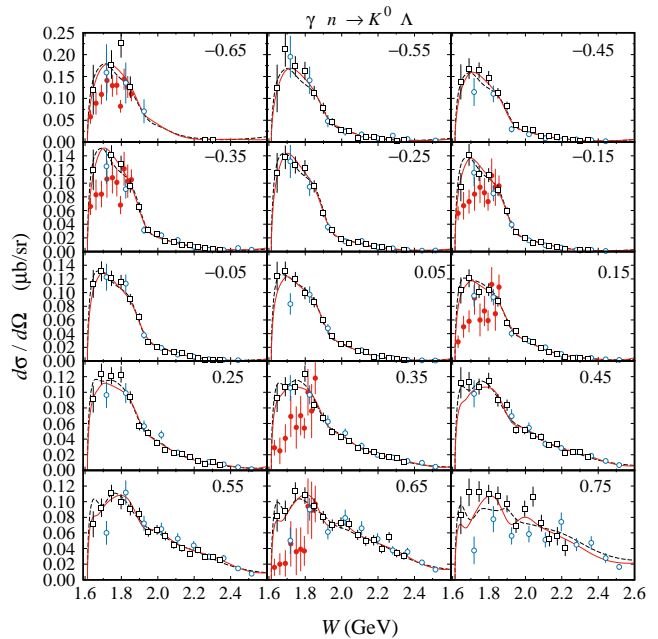


FIG. 7: Energy distribution of the $\gamma n \rightarrow K^0\Lambda$ differential cross section for different values of $\cos\theta$ shown in each panel. Notation of the curves and experimental data is as in Fig. 6.

The difference is more apparent at the forward angle, i.e., $\cos\theta = 0.75$. The angular distribution of differential cross section shown in Fig. 8 corroborates this result. In Fig. 8 we can see that the difference between the two models is more obvious in the forward and backward regions.

In general, the $K^0\Lambda$ differential cross sections also show that the inclusion of the two high-spin nucleon resonances improves the model. However, there is an important phenomenon appears in the $K^0\Lambda$ channel. As in the case of the $K^+\Lambda$ channel, the inclusion of these resonances leads to fewer structures in differential cross section, especially at the forward region (see Fig. 3). The same phenomenon is also displayed by the $K^0\Lambda$ channel as shown in Fig. 7. In this channel the previous work displays a clear structure at $W \approx 1.65$ GeV, which appears in a wide range of angular distribution, but is more apparent near forward region. The structure is eliminated by the inclusion of the two high-spin nucleon resonances. We found that this structure is very interesting because it originates from the $N(1650)$ resonance contribution and the corresponding width is less than 50 MeV (see the dashed curves in Fig. 7, especially at $\cos\theta = 0.75$). In the previous work [23] it was concluded that the structure could be a hint of the narrow resonance, which was found to have the mass of 1650 MeV.

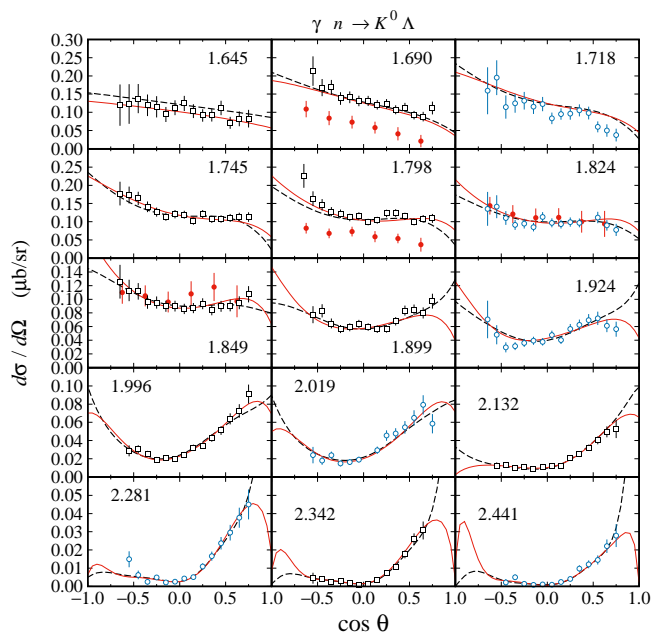


FIG. 8: As in Fig. 7, but for angular distributions. The total c.m. energy W is shown in each panel in GeV.

B. $K\Sigma$ Channel

As in the $K\Lambda$ channels, the four available channels of $K\Sigma$ photoproduction can be also simultaneously analyzed by exploiting the isospin symmetry and some information on the resonance properties from PDG [4]. Recently, we have studied these channels by using a partial wave approach for the resonance part, whereas the background part was still constructed from the covariant Feynman diagram technique [28]. The model was fitted to nearly 8000 experimental data points available from all four channels, but dominantly from the $K^+\Sigma^0$ one.

In addition, a fully covariant model to describe photoproduction of $K\Sigma$ has been also constructed by including nucleon resonances with spins up to 9/2 and the result has been submitted for publication [29]. In the present work we add the nucleon and delta resonances that are not available in this covariant model. They include the nucleon resonances with spins 11/2 and 13/2, as well as the delta resonances with spins 11/2, 13/2, and 15/2, listed in Table I. The experimental data used in this study were obtained from the CLAS, Crystal Ball, GRAAL, SAPHIR, LEPS, and SPring8 collaborations. Thus, to observe the effect of including these resonances, we will compare the result of our present work to that of the covariant model reported in Ref. [29].

Table IV lists the leading coupling constants and other background parameters extracted from the present analysis. For the sake of discussion, the present model and the model reported in Ref. [29] will be referred to as Model C and Model D, respectively. As seen from the values of χ^2/N_{dof} in Table IV, the agreement between model

TABLE IV: Extracted coupling constants and other background parameters in the $K\Sigma$ channels obtained from the present work (Model C) and the previous one (Model D) [29]. Note that error bars were not reported in Model D.

Parameter	Model C	Model D
$g_{K\Lambda N}/\sqrt{4\pi}$	-4.26 ± 0.01	-3.00
$g_{K\Sigma N}/\sqrt{4\pi}$	1.30 ± 0.25	0.90
$G_{K^*}^V/4\pi$	-0.04 ± 0.00	-0.15
$G_{K^*}^T/4\pi$	-0.03 ± 0.00	-0.21
$G_{K_1}^V/4\pi$	-0.46 ± 0.00	0.12
$G_{K_1}^T/4\pi$	0.07 ± 0.01	4.37
$r_{K_1 K \gamma}$	-2.00 ± 0.36	... ^a
$\Lambda_B(\text{GeV})$	0.84 ± 0.00	0.72
$\Lambda_R(\text{GeV})$	1.00 ± 0.00	1.25
$\theta_{\text{had}}(\text{deg})$	90.00 ± 10.11	90.0
$\phi_{\text{had}}(\text{deg})$	0.00 ± 20.05	0.00
χ^2	8729	9053
N_{par}	379	341
N_{data}	7784	7784
χ^2/N_{dof}	1.18	1.22

^aNot reported

calculation and experimental data is improved after the inclusion of the high-spin nucleon and delta resonances. The result is clearly expected, because the addition of resonances increases the free parameters in the model. Table IV also shows that the inclusion of the high-spin resonances helps to increase the hadronic form factor cut-off of the Born terms as in the $K\Lambda$ case.

1. $K^+\Sigma^0$ Channel

Among all possible $K\Sigma$ isospin channels, the $\gamma p \rightarrow K^+\Sigma^0$ channel has the most abundant experimental data. This is understandable since, as the production of $K^+\Lambda$, the production of $K^+\Sigma^0$ is relatively easier to measure due to stable proton target and relatively simpler technique to measure the decay of Λ or Σ^0 hyperon in the final states. The experimental data mentioned here include those obtained from the Crystal Ball (at MAMI) [21], CLAS [16, 30, 31], GRAAL [32], LEPS, SAPHIR and SPring8 collaborations.

Figure 9 shows the comparison between the calculated total cross sections before and after the inclusion of the high-spin resonances, where the prediction of Kaon-Maid is also displayed to show the improvement made by the current models. It is seen that the prediction of Model C (solid red curve) is practically similar to that of Model D (dashed black curve). The difference between both models is very subtle and can be seen only at $W \approx 2.0$ GeV and $W \approx 2.25$ GeV. Overall, both models fit nicely the experimental data, with an exception at $W \gtrsim 2.15$ GeV, where we observe that there is a discrepancy problem in

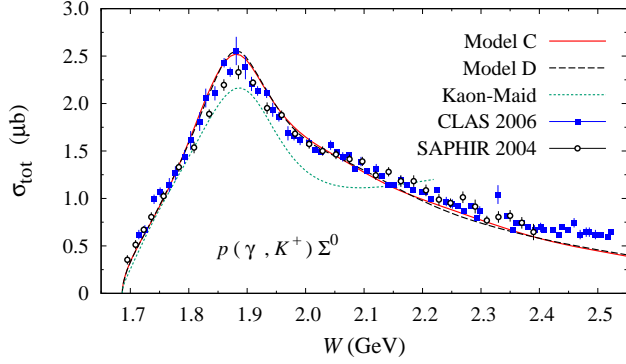


FIG. 9: Total cross section of the $\gamma p \rightarrow K^+ \Sigma^0$ channel. Notation of the curves and experimental is given in the figure. Data shown in this figure were not used in the fitting process of the present model.

the existing experimental data of total and differential cross sections. This problem will be clarified later when we discuss the result for differential cross section.

Comparison between differential cross sections obtained from the two models is shown in Figs. 10 and 11. The energy distribution of differential cross section shown in Fig. 10 reveals that the difference between the two models is most obvious at $\cos \theta = 0.95$. At this for-

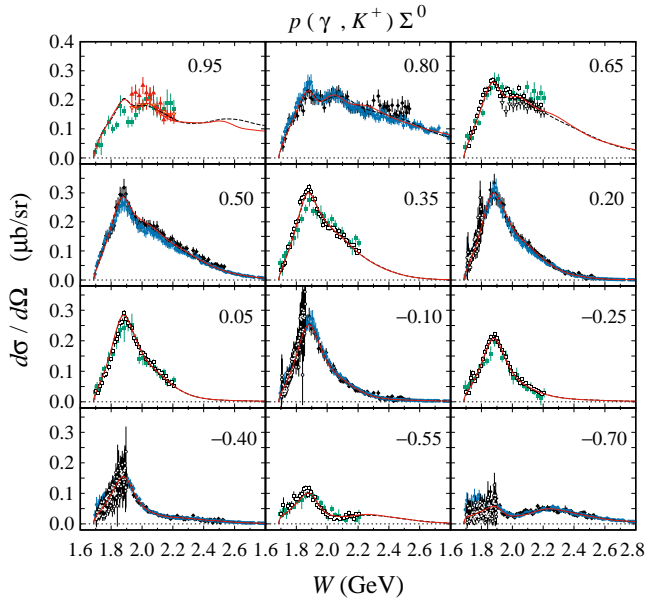


FIG. 10: Energy distributions of the $\gamma p \rightarrow K^+ \Sigma^0$ differential cross section for different values of $\cos \theta$. Shown in the figure are the results obtained from Model C (solid red curve) and Model D (dashed black curve). Experimental data shown are taken from the CLAS 2004 (open squares [30]), SAPHIR 2004 (solid squares [33]), CLAS 2006 (solid diamonds [16]), LEPS 2006 (solid triangles [19] and open inverted triangles [34]), CLAS 2007 (solid circles [31]), and Crystal Ball ([21]) collaborations.

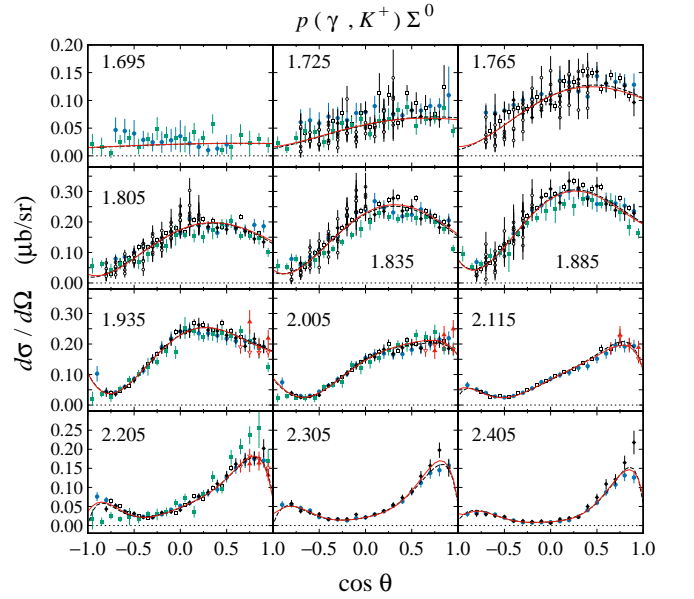


FIG. 11: As in Fig. 10, but for angular distribution. The corresponding total c.m. energy W is shown in each panel in GeV.

ward angle we can see that the inclusion of the high-spin resonances yields at least two structures in differential cross section at the $W \geq 2.6$ GeV, which can be traced back to the resonance masses.

Furthermore, the second peak in differential cross section becomes more apparent and much closer to experimental data after the inclusion of these resonances. This peak still clearly appears at $\cos \theta = 0.80$ and 0.65 , and quickly disappears as we move to larger kaon angles. We have investigated the origin of this second peak and found that it is due to the $\Delta(2000)F_{35}$ resonance.

In addition, we also observe a third peak at $W \approx 2.3$ GeV, which originates from the $N(2290)G_{19}$ state with spin $9/2$, has positive parity, and earns a status of four-star in the Particle Data Book [4]. Interestingly, this state appears in the $K^+ \Sigma^0$ channel after the inclusion of higher nucleon resonances. This peak also quickly disappears as we increase the kaon angle, but appears again in the backward angles. In the latter, both models are in agreement with each other.

The angular distributions of differential cross section shown in Fig. 11 support this finding. In general, the agreement with experimental data are similar for the two models. In the case when the experimental data from different collaborations are scattered, the models try to reproduce their average.

2. $K^0 \Sigma^+$ Channel

The $K^0 \Sigma^+$ channel is the last channel measured for the proton target. Although proton is stable, detection of the

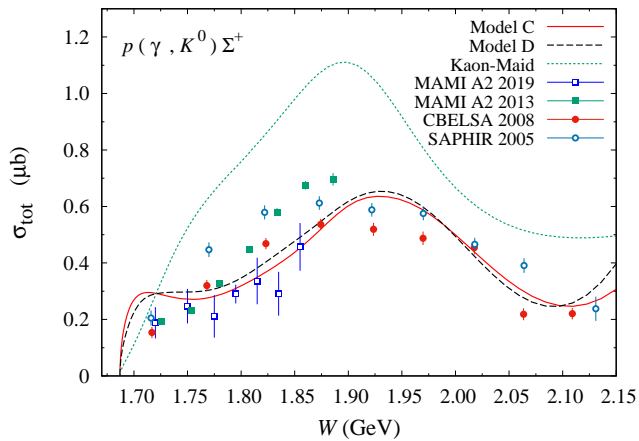


FIG. 12: Total cross section for the $\gamma p \rightarrow K^0 \Sigma^+$ process obtained from the present and previous models. Experimental data are obtained from the SAPHIR 2005 [35], CBELSA 2008 [36], MAMI A2 2013 [37], and MAMI A2 2019 [15] collaborations. All data shown in this figure were not used in the present analysis.

neutral kaon and positively charged Σ hyperon in the final state is more challenging. Figure 12 shows the $K^0 \Sigma^+$ total cross sections obtained from both models, as well as Kaon-Maid for comparison. Obviously, the three models display different shapes of total cross section, which originate from different nucleon and delta resonances used in the models. We note that experimental data for this channel are relatively scattered, especially in the energy range $1.77 \lesssim W \lesssim 1.90$ GeV, where the new SAPHIR data are almost 50% smaller than the older SAPHIR data. Fortunately, near the production threshold all data are in agreement with each other and, interestingly, closer to the prediction of Kaon-Maid. Nevertheless, at this point we still observe that the inclusion of higher-spin resonances improves the model prediction. Furthermore, as shown in Fig. 12, very close to the threshold the predictions of the three models are very different. While the predicted cross section of Kaon-Maid is slowly increasing with energy, the calculated cross section of the present model (Model C) is rising steeply and reveals the contributions of resonances with masses near 1.7 GeV. We note that there are four nucleon resonances and one delta resonance to this end. As stated in Ref. [38], experimental data near the threshold region are very crucial to understand the production mechanism and related phenomenological applications [39].

Despite the fact that there are limited data available for this reaction, the agreement between model calculation and experimental data increases significantly with the inclusion of high-spin resonances. As in the case of previous channels, the inclusion of high-spin resonances leads also to a number of structures in the total cross sections, as clearly shown in Fig. 12.

The limited number of experimental data for the $K^0 \Sigma^+$ photoproduction clearly impose a strong constraint on

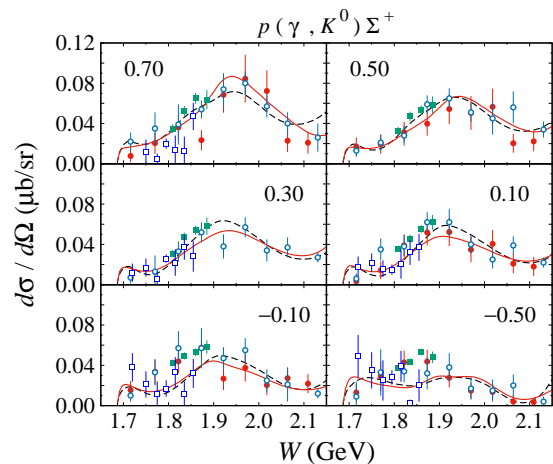


FIG. 13: Energy distribution of the $\gamma p \rightarrow K^0 \Sigma^+$ differential cross section calculated from Models C and D for different values of $\cos \theta$, compared with available experimental data. Notation of the curves and experimental data is as in Fig. 12.

the range of validity of our present model. Figure 13 obviously shows that the available data are relatively scattered, with apparent peak at $W \approx 1.95$ GeV. This peak is more obvious in the forward regions. Furthermore, in this figure we can also observe that the inclusion of high-spin resonances eliminates the small structure at $W \approx 1.85$ GeV and emphasizes the contribution of resonances with $m \approx 1.7$ GeV as in the case of total cross section. More experimental data are strongly required, especially at these energy points, to clarify the effects of the inclusion of high-spin resonances in the present model.

The angular distributions of differential cross section shown in Fig. 14 clear up the difference between Models C and D, which is visible in the whole angles covered by experimental data. The improvement of the model after including the high-spin resonances is relatively unclear due to the scattered experimental data. In general, the inclusion of the high-spin resonances slightly improves the agreement between model calculation and experimental data. Both Figs. 13 and 14 indicate that the present model prefers the new MAMI A2 2019 data set [15] in the energy range $1.8 \lesssim W \lesssim 1.9$ GeV, where experimental data from different collaborations are significantly scattered.

3. $K^+ \Sigma^-$ Channel

The $K^+ \Sigma^-$ photoproduction channel has nearly 300 experimental data points in the form of differential cross section [34, 40] and photon asymmetry [34]. These data were included in the fitting process. Thus, the total cross sections shown in Fig. 15 are pure prediction and cannot be compared with experimental measurement. Nevertheless, we still can see the small effect of the higher-

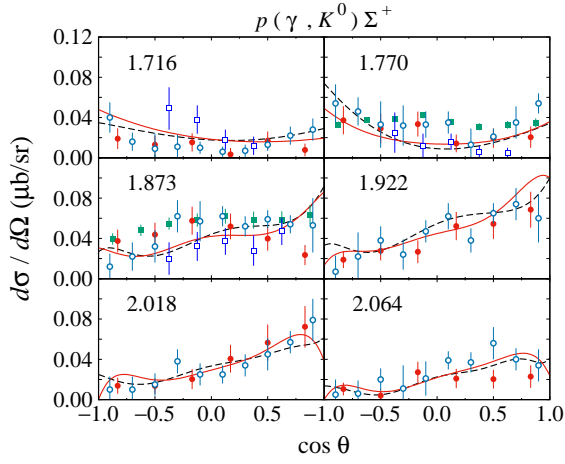


FIG. 14: As in Fig. 13, but for angular distribution. The corresponding total c.m. energy W in GeV is shown in each panel.

spin resonances near the $K^+\Sigma^-$ threshold, as in the case of $K^0\Sigma^+$ channel, and at high energy $W \gtrsim 2.1$ GeV where no experimental data are available to constrain the model. Otherwise, both models C and D show similar trend.

The calculated $K^+\Sigma^-$ differential cross sections obtained from both models are compared with experimental data in Fig. 16. This figure reveals that the origin of the structures shown in the total cross section. Near the threshold the peak appears in the whole angular distribution, whereas the difference between the two models at high energy originates from the backward angles. It is interesting to note that at high energy the inclusion of the high-spin resonances slightly increases the cross section, but in the backward region this situation dramatically changes (see the panel with $\cos\theta = -0.65$).

For completeness, we have also checked the angular distribution of $K^+\Sigma^-$ differential cross section. Figure 17 shows the comparison between both models and experimental data. Similar to Fig. 16, we can see that the difference between models C and D is also small, except

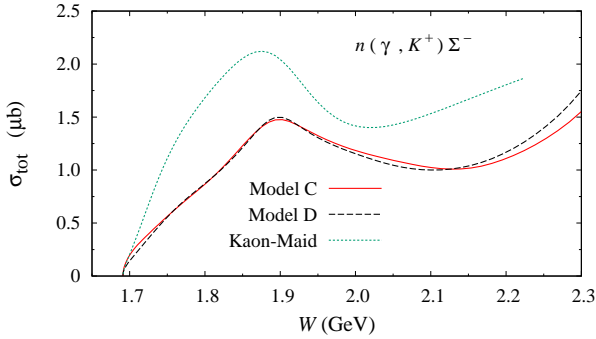


FIG. 15: Calculated total cross section of $\gamma n \rightarrow K^+\Sigma^-$ process.

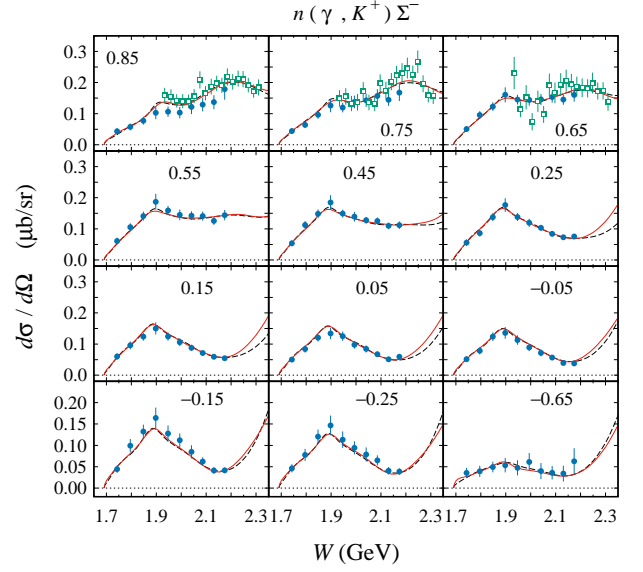


FIG. 16: Energy distribution of the $\gamma n \rightarrow K^+\Sigma^-$ differential cross section. Notation of the curves is as in Fig. 15. Experimental data are obtained from the LEPS 2006 [34] and CLAS 2010 [40] collaborations.

at high energy, i.e. at $W = 2.174$ GeV and backward angle.

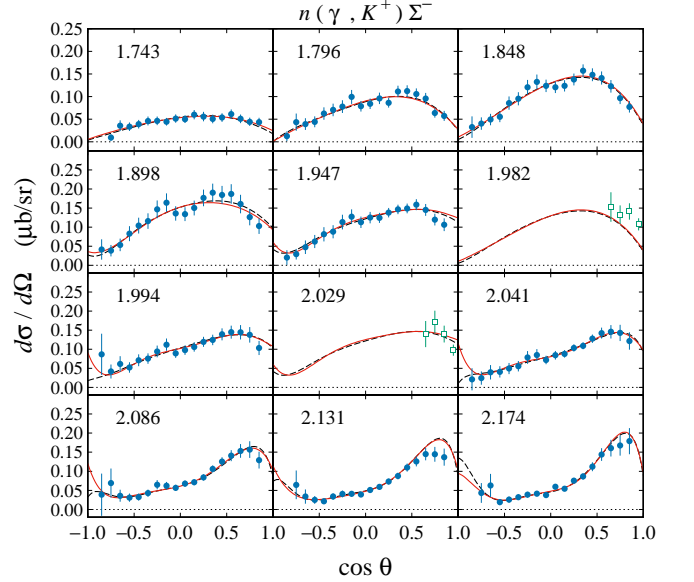


FIG. 17: As in Fig. 16, but for angular distribution.

4. $K^0\Sigma^0$ channel

The $K^0\Sigma^0$ channel has very limited experimental data. They were obtained by the MAMI A2 2018 collabora-

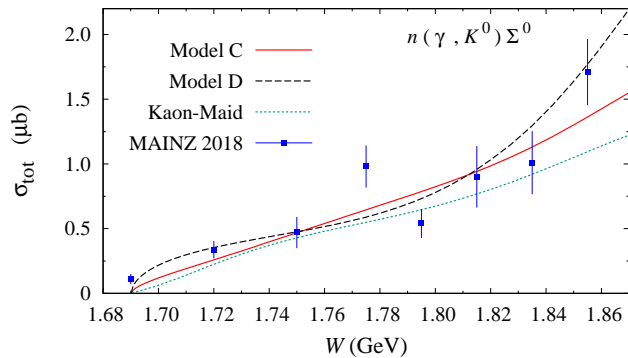


FIG. 18: Total cross section of $\gamma n \rightarrow K^0 \Sigma^0$ process. Experimental data [15] shown in this figure were not included in the fitting process of the present model.

tion by measuring photoproduction of neutral kaon on a deuteron target. Although the number is very limited, the existence of experimental data in this channel significantly helps to constrain the prediction of the present model. Figure 18 shows the comparison between calculated total cross sections obtained from previous and present models and experimental data. It can be seen that the inclusion of the high-spin resonances improves the model, although the cross section trend is relatively well reproduced by the three models. The importance of the nucleon and delta resonances with $m \approx 1.7$ GeV is slightly shown by Model D near the production threshold.

As shown in Fig. 18 the total cross sections increase monotonically with increasing energy. In fact, the predicted total cross section of the present model is more than $3 \mu\text{b}$ at $W \approx 2$ GeV, which seems to be unrealistic if we compare it with those of the neutral kaon productions shown in Figs. 6 and 12. Thus, total cross section data up to 2.5 GeV are very important to this end.

Figures 19 and 20 compare the calculated differential cross sections obtained from the previous and present models with experimental data. Figure 19 shows that models C and D start to differ at $W \approx 1.86$ GeV, where no experimental data are available to constrain them. The inclusion of the high-spin resonances in this channel improves the cross section divergence, which is urgently required in forward regions. Interestingly, the two models predict a resonance structure above this energy point, albeit with different positions. Certainly, experimental data in the energy range $1.8 \lesssim W \lesssim 2.2$ GeV are very important to determine which resonance is responsible for this structure.

The angular distributions of differential cross section shown in Fig. 20 reveals that the cross section of the $K^0 \Sigma^0$ photoproduction has backward-peaking behavior. This indicates the dominance of u -channel in this process, which is easily understood from the fact that this process does not have a t -channel in the Born terms since a neutral kaon cannot interact with real photon.

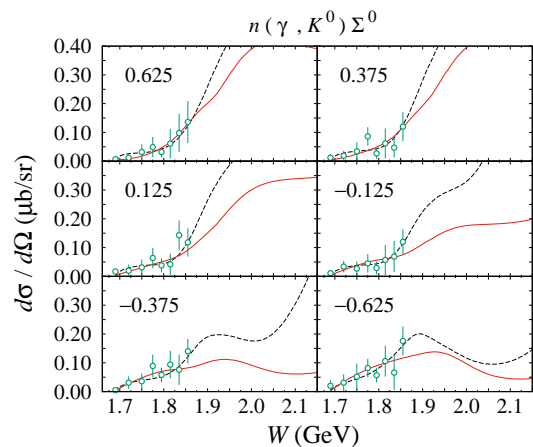


FIG. 19: Energy distribution of the $\gamma n \rightarrow K^0 \Sigma^0$ differential cross section. Notation for the curves and experimental data is as in Fig. 18.

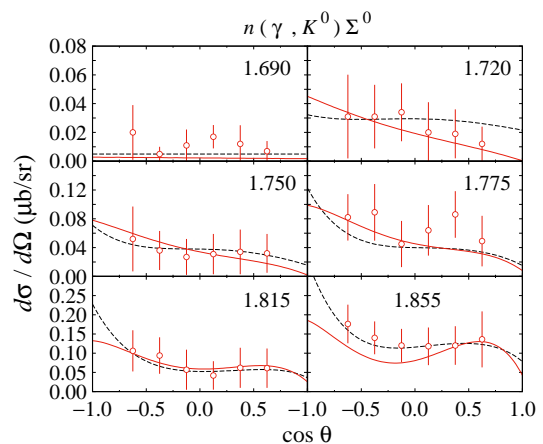


FIG. 20: As in Fig. 19, but for angular distribution.

C. Extracted Resonance Properties

Having investigated the effect of high-spin resonances on our models, we are ready to discuss the resonance properties, i.e., their masses and widths, at their pole positions, before and after including the high-spin resonances. Note that during the fitting process we allowed the resonance masses and widths to vary within the estimated error bars of PDG. In Table V we show the resonance masses and widths evaluated at their pole positions extracted from the present and previous works, compared with those listed by PDG [4]. Note that for the $N(2600)I_{1,11}$, $N(2700)K_{1,13}$, $\Delta(2750)I_{3,13}$ and $\Delta(2950)K_{3,15}$ resonances, the PDG does not have any information yet. Therefore, in this case, the result shown in Table V provides the first estimate for these resonances.

In the $K\Lambda$ photoproduction the agreement between the extracted properties of nucleon resonances and those of PDG is in general from fair to good. The same situation is also seen in the $K\Sigma$ one. Good agreement with the

TABLE V: Masses and widths of nucleon and Δ resonances evaluated at the pole position in MeV, obtained from the present work (Models A and C), previous works (Models B [3] and D [29]) and PDG [4]. The status of resonances is due to the PDG [4].

Resonances	Status	PDG		Model A		Model B		Model C		Model D	
		m_{pole}	Γ_{pole}	m_{pole}	Γ_{pole}	m_{pole}	Γ_{pole}	m_{pole}	Γ_{pole}	m_{pole}	Γ_{pole}
$N(1440)P_{11}$	****	1370 ± 10	175 ± 15	1305 ± 27.9	173 ± 46.0	1305	173	1355 ± 5.2	208 ± 7.2	1324	188
$N(1520)D_{13}$	****	1510 ± 5	110 $^{+10}_{-5}$	1488 ± 3.5	112 ± 10.8	1495	101	1487 ± 4.4	112 ± 11.7	1489	100
$N(1535)S_{11}$	****	1510 ± 10	130 ± 20	1508 ± 15.0	169 ± 26.0	1475	162	1474 ± 15.2	225 ± 17.3	1530	129
$N(1650)S_{11}$	****	1655 ± 15	135 ± 35	1599 ± 1.5	230 ± 5.0	1612	232	1600 ± 18.1	230 ± 4.7	1664	176
$N(1675)D_{15}$	****	1660 ± 5	135 $^{+15}_{-10}$	1639 ± 0.0	147 ± 0.2	1640	147	1629 ± 2.7	164 ± 14.1	1643	136
$N(1680)F_{15}$	****	1675 $^{+5}_{-10}$	120 $^{+15}_{-10}$	1644 ± 0.9	119 ± 0.6	1651	123	1653 ± 2.9	121 ± 7.6	1667	98
$N(1700)D_{13}$	***	1700 ± 50	200 ± 100	1668 ± 0.3	155 ± 0.2	1692	158	1637 ± 0.6	183 ± 0.6	1630	111
$N(1710)P_{11}$	****	1700 ± 20	120 ± 40	1658 ± 0.9	120 ± 2.9	1657	175	1676 ± 0.8	71 ± 3.0	1705	47
$N(1720)P_{13}$	****	1675 ± 15	250 $^{+150}_{-100}$	1632 ± 0.1	220 ± 0.4	1648	193	1578 ± 0.7	242 ± 1.5	1665	300
$N(1860)F_{15}$	**	1830 $^{+120}_{-60}$	250 $^{+150}_{-50}$	1874 ± 0.2	226 ± 0.4	1862	217	1836 ± 0.4	241 ± 0.7	1787	156
$N(1875)D_{13}$	***	1900 ± 50	160 ± 60	1840 ± 0.2	230 ± 1.0	1815	222	1765 ± 4.9	223 ± 0.7	1757	219
$N(1880)P_{11}$	***	1860 ± 40	230 ± 50	1753 ± 1.7	325 ± 0.7	1785	298	1836 ± 4.8	278 ± 3.2	1831	166
$N(1895)S_{11}$	****	1910 ± 20	110 ± 30	1874 ± 0.2	299 ± 0.4	1876	224	1848 ± 0.1	320 ± 0.4	1893	90
$N(1900)P_{13}$	****	1920 ± 20	150 ± 50	1846 ± 0.2	265 ± 0.4	1865	256	1874 ± 0.7	186 ± 0.8	1899	239
$N(1990)F_{17}$	**	2030 ± 65	240 ± 60	1935 ± 0.8	249 ± 1.3	1867	240	1916 ± 0.5	225 ± 1.2	2044	273
$N(2000)F_{15}$	**	2030 ± 40	380 ± 60	1858 ± 0.2	264 ± 0.5	1932	273	1898 ± 1.2	260 ± 2.6	1978	232
$N(2060)D_{15}$	***	2070 $^{+60}_{-50}$	400 $^{+30}_{-50}$	1950 ± 0.7	400 ± 0.3	1856	341	1951 ± 1.2	401 ± 1.1	1968	334
$N(2120)D_{13}$	***	2100 ± 50	280 ± 60	1963 ± 0.7	354 ± 0.1	1884	354	1957 ± 0.7	385 ± 1.5	2029	274
$N(2190)G_{17}$	****	2100 ± 50	400 ± 100	2014 ± 0.6	241 ± 0.3	2025	244	2059 ± 30.7	256 ± 64.4	2142	211
$N(2220)H_{19}$	****	2170 $^{+30}_{-40}$	400 $^{+80}_{-40}$	2047 ± 0.4	220 ± 2.0	2020	228	2114 ± 18.4	240 ± 53.0	2131	202
$N(2250)G_{19}$	****	2200 ± 50	420 $^{+80}_{-80}$	2138 ± 0.5	284 ± 4.9	2085	265	2138 ± 2.2	285 ± 4.6	2193	219
$N(2600)I_{1,11}$	***	2318 ± 1.9	272 ± 33.9	2389 ± 11.4	310 ± 34.9
$N(2700)K_{1,13}$	**	2393 ± 3.4	247 ± 18.0	2457 ± 17.7	253 ± 41.8
$\Delta(1232)P_{33}$	****	1210 ± 1	100 ± 2	1209 ± 1.7	82 ± 5.2	1205	82
$\Delta(1600)P_{33}$	****	1510 ± 50	270 ± 70	1444 ± 64.3	170 ± 52.5	1457	168
$\Delta(1620)S_{31}$	****	1600 ± 10	120 ± 20	1565 ± 15.6	140 ± 20.2	1598	152
$\Delta(1700)D_{33}$	****	1665 ± 25	250 ± 50	1616 ± 3.6	221 ± 1.2	1646	161
$\Delta(1900)S_{31}$	***	1865 ± 35	240 ± 60	1760 ± 0.3	375 ± 1.0	1938	330
$\Delta(1905)F_{35}$	****	1800 ± 30	300 ± 40	1772 ± 4.7	228 ± 15.3	1797	212
$\Delta(1910)P_{31}$	****	1860 ± 30	300 ± 100	1836 ± 0.4	351 ± 0.9	1859	317
$\Delta(1920)P_{33}$	***	1900 ± 50	300 ± 100	1758 ± 4.0	281 ± 7.7	1893	193
$\Delta(1930)D_{35}$	***	1880 ± 40	280 ± 50	1850 ± 0.2	314 ± 0.7	1933	199
$\Delta(1940)D_{33}$	**	1950 ± 100	350 ± 150	1878 ± 0.2	334 ± 1.1	1880	349
$\Delta(1950)F_{37}$	****	1880 ± 10	240 ± 20	1835 ± 2.3	208 ± 5.7	1848	208
$\Delta(2000)F_{35}$	**	2150 ± 100	350 ± 100	1844 ± 16.8	275 ± 42.4	2081	328
$\Delta(2300)H_{39}$	**	2370 ± 80	420 ± 160	2318 ± 4.7	288 ± 4.3	2341	200
$\Delta(2400)G_{39}$	**	2260 ± 60	320 ± 160	2282 ± 1.2	386 ± 4.1	2409	329
$\Delta(2420)H_{3,11}$	****	2400 ± 100	450 ± 100	2302 ± 60.4	288 ± 118.3
$\Delta(2750)I_{3,13}$	**	2454 ± 28.3	309 ± 64.3
$\Delta(2950)K_{3,15}$	**	2572 ± 33.6	297 ± 88.2

PDG values is observed in the case of the $N(1520)D_{13}$ and $\Delta(1232)P_{33}$ resonances. Certain resonances with low rating status, e.g., the $N(1875)D_{13}$, $N(2000)F_{15}$ and $\Delta(1900)S_{31}$ states, show notable deviation from the PDG value. This indicates that the less-established resonances

tend to produce the resonance properties that significantly deviates from the PDG values. From Table V it is also apparent that the nucleon properties obtained from Model A have a better agreement with the PDG values, in contrast to Model B, especially for the resonances

TABLE VI: Breit-Wigner mass and width of nucleon and Δ resonances in MeV from present work (Models A and C) previous works (Models B [3] and D [29]) and PDG [4].

Resonances	PDG		Model A ($K\Lambda$)		Model B ($K\Lambda$)		Model C ($K\Sigma$)		Model D ($K\Sigma$)	
	Mass	Width	Mass	Width	Mass	Width	Mass	Width	Mass	Width
$N(1440)P_{11}$	1440 \pm 30	350 \pm 100	1410 \pm 49	450 \pm 41.3	1410	450	1470 \pm 8.0	450 \pm 7.6	1420	450
$N(1520)D_{13}$	1515 \pm 5	110 \pm 10	1520 \pm 2.1	120 \pm 12.3	1520	100	1519 \pm 0.9	120 \pm 13.3	1510	125
$N(1535)S_{11}$	1530 \pm 15	150 \pm 25	1545 \pm 3.7	125 \pm 48.5	1545	175	1545 \pm 27.7	175 \pm 32.7	1545	125
$N(1650)S_{11}$	1650 \pm 15	125 \pm 25	1545 \pm 2.5	150 \pm 0.8	1645	159	1635 \pm 29.4	150 \pm 9.8	1670	170
$N(1675)D_{15}$	1675 \pm 15	145 \pm 15	1635 \pm 0.1	130 \pm 0.3	1680	130	1680 \pm 9.6	160 \pm 21.2	1670	165
$N(1680)F_{15}$	1685 \pm 5	120 $^{+10}_{-5}$	1680 \pm 1.5	115 \pm 0.7	1690	120	1690 \pm 1.0	115 \pm 9.9	1686	120
$N(1700)D_{13}$	1720 $^{+80}_{-70}$	200 \pm 100	1712 \pm 0.5	134 \pm 0.5	1731	102	1706 \pm 1.0	201 \pm 0.9	1650	129
$N(1710)P_{11}$	1710 \pm 30	140 \pm 60	1708 \pm 0.5	182 \pm 3.0	1733	1250	1697 \pm 0.4	80 \pm 2.8	1710	50
$N(1720)P_{13}$	1720 $^{+30}_{-40}$	250 $^{+150}_{-100}$	1703 \pm 0.5	208 \pm 0.6	1700	2189	1687 \pm 0.0	340 \pm 2.3	1750	400
$N(1860)F_{15}$	1928 \pm 21	376 \pm 58	1980 \pm 0.7	235 \pm 0.8	1960	220	1971 \pm 1.0	337 \pm 1.2	1829	220
$N(1875)D_{13}$	1875 $^{+45}_{-25}$	200 $^{+150}_{-80}$	1918 \pm 1.4	177 \pm 2.2	1858	180	1850 \pm 8.7	213 \pm 0.9	1820	320
$N(1880)P_{11}$	1880 \pm 50	300 \pm 100	1930 \pm 4.4	400 \pm 1.2	1915	280	1930 \pm 9.6	200 \pm 7.7	1856	180
$N(1895)S_{11}$	1895 \pm 25	120 $^{+80}_{-40}$	1903 \pm 0.7	142 \pm 1.2	1893	106	1884 \pm 0.7	157 \pm 1.4	1893	90
$N(1900)P_{13}$	1920 \pm 30	200 $^{+120}_{-100}$	1920 \pm 0.6	169 \pm 1.1	1930	151	1907 \pm 1.6	100 \pm 1.9	1930	250
$N(1990)F_{17}$	2020 $^{+80}_{-70}$	300 \pm 100	2057 \pm 2.9	245 \pm 2.7	1995	265	2013 \pm 1.5	200 \pm 2.5	2125	400
$N(2000)F_{15}$	2060 \pm 30	390 \pm 55	2030 \pm 0.4	445 \pm 0.9	2090	338	2046 \pm 0.9	335 \pm 4.8	2044	335
$N(2060)D_{15}$	2100 $^{+100}_{-70}$	400 $^{+50}_{-100}$	2200 \pm 2.2	450 \pm 0.8	2060	450	2200 \pm 2.7	450 \pm 2.7	2060	450
$N(2120)D_{13}$	2120 $^{+40}_{-60}$	300 $^{+60}_{-40}$	2126 \pm 1.4	275 \pm 0.3	2075	375	2160 \pm 1.6	345 \pm 4.2	2075	305
$N(2190)G_{17}$	2180 \pm 40	400 \pm 100	2159 \pm 1.8	300 \pm 0.5	2181	300	2216 \pm 5.1	300 \pm 127.8	2200	300
$N(2220)H_{19}$	2250 \pm 50	400 $^{+100}_{-50}$	2200 \pm 2.5	350 \pm 3.1	2200	500	2284 \pm 24.2	350 \pm 92.7	2204	369
$N(2250)G_{19}$	2280 $^{+40}_{-30}$	500 $^{+100}_{-200}$	2320 \pm 1.8	300 \pm 11.2	2283	300	2320 \pm 2.2	300 \pm 10.4	2250	300
$N(2600)I_{1,11}$	2600 $^{+150}_{-50}$	650 \pm 150	2573 \pm 6.9	500 \pm 61.8	2750 \pm 7.8	800 \pm 59.1
$N(2700)K_{1,13}$	2612 \pm 45	350 \pm 50	2621 \pm 3.3	400 \pm 17.8	2675 \pm 9.6	300 \pm 89.9
$\Delta(1232)P_{33}$	1232 \pm 2	117 \pm 3	1234 \pm 2.8	114 \pm 4.0	1230	120
$\Delta(1600)P_{33}$	1570 \pm 70	250 \pm 50	1500 \pm 99	200 \pm 68.6	1500	220
$\Delta(1620)S_{31}$	1610 \pm 20	130 \pm 20	1590 \pm 28.8	110 \pm 30.3	1600	150
$\Delta(1700)D_{33}$	1710 \pm 20	300 \pm 800	1730 \pm 5.9	355 \pm 1.2	1686	213
$\Delta(1900)S_{31}$	1860 $^{+80}_{-20}$	250 \pm 70	1920 \pm 1.2	320 \pm 2.7	1920	325
$\Delta(1905)F_{35}$	1880 $^{+30}_{-25}$	330 $^{+70}_{-60}$	1910 \pm 6.7	400 \pm 21.9	1878	400
$\Delta(1910)P_{31}$	1900 \pm 50	300 \pm 100	1950 \pm 1.0	242 \pm 2.5	1910	340
$\Delta(1920)P_{33}$	1920 \pm 50	300 \pm 60	1970 \pm 1.2	360 \pm 14.5	1908	195
$\Delta(1930)D_{35}$	1950 \pm 50	300 \pm 100	2000 \pm 0.6	313 \pm 1.5	1963	220
$\Delta(1940)D_{33}$	2000 \pm 60	400 \pm 100	2044 \pm 1.3	330 \pm 2.7	1994	520
$\Delta(1950)F_{37}$	1930 \pm 15	285 \pm 50.0	1934 \pm 2.2	235 \pm 9.7	1915	335
$\Delta(2000)F_{35}$	2015 \pm 24	500 \pm 52	2039 \pm 6.8	552 \pm 65.6	2192	525
$\Delta(2300)H_{39}$	2400 \pm 125	425 \pm 150	2525 \pm 12	275 \pm 10.6	2393	275
$\Delta(2400)G_{39}$	2643 \pm 141	895 \pm 432	2641 \pm 4.2	544 \pm 10.1	2504	463
$\Delta(2420)H_{3,11}$	2300 \pm 150	500 \pm 200	2515 \pm 12.5	300 \pm 281.3
$\Delta(2750)I_{3,13}$	2794 \pm 80	350 \pm 100	2760 \pm 2.3	450 \pm 141.0
$\Delta(2950)K_{3,15}$	2990 \pm 100	330 \pm 100	2890 \pm 129.2	430 \pm 193.3

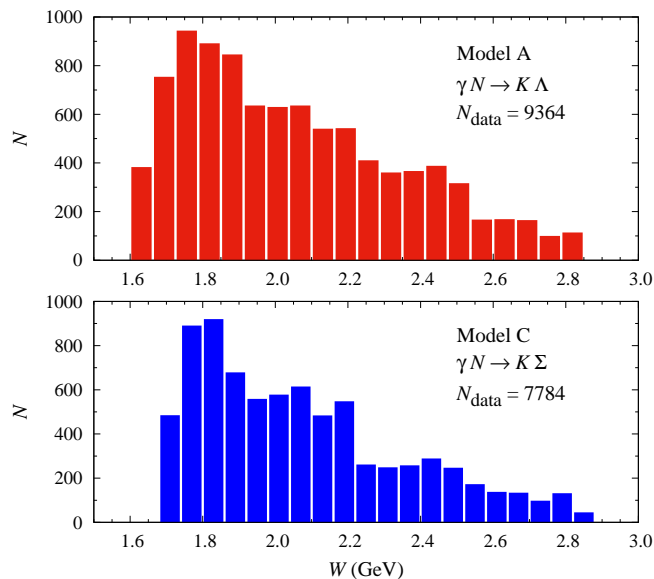


FIG. 21: Energy distributions of the experimental data used in the fitting process of Model A ($K\Lambda$ photoproduction) and model C ($K\Sigma$ photoproduction).

whose masses are less than 2000 MeV, as well as for the $N(2220)H_{19}$ and $N(2250)G_{19}$ states. Furthermore, we can also observe that Model D seems to produce higher extracted masses than Model C. On the other hand, the calculated widths obtained from Model C are found to be closer to the PDG values, except for the $N(2190)G_{17}$, $N(2220)H_{19}$ and $N(2250)G_{19}$ resonances.

The difference between the mass of $N(2700)K_{1,13}$ resonance extracted from the $K\Lambda$ and $K\Sigma$ channels seems to be large, i.e., nearly 100 MeV. Furthermore, the extracted masses are smaller than the Breit-Wigner ones, as can be seen in Table V. Nevertheless, the masses and widths of the two resonances extracted in this work provide the first prediction of their pole properties.

In contrast to the $N(2600)I_{1,11}$ and $N(2700)K_{1,13}$ resonances, the extracted properties of the $\Delta(2420)H_{3,11}$ resonance are in a good agreement with the PDG values. For the other two high-spin Δ resonances, i.e., $\Delta(2750)I_{3,13}$ and $\Delta(2950)K_{3,15}$ states, the PDG does not have data for comparison. For both $\Delta(2750)I_{3,13}$ and $\Delta(2950)K_{3,15}$ resonances the extracted masses at the pole position are much smaller than those of the Breit-Wigner. Since the resonances affect the cross section and other polarization observables only at high energies, i.e., $W \gtrsim 2.7$ GeV, a study devoted for high energy photoproduction would be very relevant to this end. This would be also in line with the 12 GeV JLab experiments that are currently in progress.

In Tables V and VI we have also included the error bars both from PDG and the present work. Note that the previous works did not report the uncertainties in the extracted resonance masses and widths. The quoted error bars of the present work originate from the CERN-

MINUIT output used for the fitting process, where we employed the MIGRAD minimizer that produces both estimated error bars of the fitted parameters and error matrix [41].

The error bars obtained from the MINUIT indicate the flexibility of the model to the variation of the resonance masses and widths to reproduce the data, i.e., the larger the error bars the more flexible the model. As a consequence, in the energy region where precise experimental data are abundantly available the error bars are forced to be small. Thus, we might expect that the error bars are large below and near the threshold region and for $W \gtrsim 2.4$ GeV (see Fig. 21). This is proven in Table V, where we can see that relatively larger error bars are obtained in Model A ($K\Lambda$ photoproduction with $W^{\text{thr.}} \approx 1610$ MeV) for the $N(1440)P_{11}$, $N(1520)D_{13}$, $N(1535)S_{11}$ resonances. In Model C ($K\Sigma$ photoproduction with $W^{\text{thr.}} \approx 1690$ MeV) three more resonances, i.e., the $N(1650)S_{11}$, $N(1675)D_{15}$, and $N(1680)F_{15}$ states, also exhibit this phenomenon. Only the $\Delta(1232)P_{33}$ resonance has very small error bars, since PDG has estimated this resonance with very precise mass and width, whereas during the fitting process we allowed these parameters to vary within the PDG uncertainties. In the higher energy region we observe that all baryon resonances with $m_R \gtrsim 2400$ MeV show the relatively larger error bars.

In conclusion, we have observed that the addition of the high-spin resonances, with spins from 11/2 up to 15/2, in our isobar models improves the agreement between their pole properties extracted in this work and those listed by PDG.

IV. SUMMARY AND CONCLUSION

We have derived the spin-11/2, -13/2, and -15/2 resonance amplitudes for kaon photoproduction off the nucleon by using the covariant Feynman diagrammatic technique. For this purpose we made use of the consistent interaction Lagrangians proposed by Pascalutsa and Vrancx *et al.*, as well as the formulation of spin-(n+1/2) resonance propagator put forwarded by Vrancx *et al.* We have studied the effect of high-spin resonances in the kaon photoproduction processes by including the $N(2600)I_{1,11}$ and $N(2700)K_{1,13}$ states in our previous model for $K\Lambda$ photoproduction and the $N(2600)I_{1,11}$, $N(2700)K_{1,13}$, $\Delta(2420)H_{3,11}$, $\Delta(2750)I_{3,13}$, and $\Delta(2950)K_{3,15}$ states in our previous model developed for $K\Sigma$ photoproduction. In general, the inclusion of these high-spin resonances improves the agreement between model calculations and experimental data, which is indicated by the smaller values of χ^2 in all isospin channels. The inclusion of the high-spin resonances also helps to overcome the problem of resonance-dominated model, since the inclusion increases the hadronic form factor cutoff of the Born terms and, therefore, increases the role of the Born terms in both $K\Lambda$ and $K\Sigma$ models. Specifically, in the $K^+\Lambda$ channel the inclusion leads to fewer resonance structures

in the cross sections and polarization observables. The effect is significant in the high energy differential cross section, near the resonance masses and at forward direction. Different from the $K^+\Lambda$ channel, the effect in the $K^0\Lambda$ channel is more obvious and can be observed in both low and high energy regions. Furthermore, in this channel the effect is found to be large in both forward and backward angles. In the $K^+\Sigma^0$ channel the effect is only significant in the forward region, where a number of resonance structures appear after including the high-spin resonances. Two of them are important to note here, i.e., the $\Delta(2000)F_{35}$ and $N(2290)G_{19}$ resonances, which are responsible for the second and third peaks in the $K^+\Sigma^0$ differential cross section. In contrast to the $K^+\Sigma^0$ channel, the $K^0\Sigma^+$ channel is found to be sensitive to these high-spin resonances. In this case, the effect can be ob-

served in the whole energy range covered by experimental data and the whole angular distribution. The effect is, however, not observed in the $K^+\Sigma^-$ and $K^0\Sigma^0$ channels, at least in the whole kinematics where experimental data are available. Finally, we found that the addition of the high-spin resonances leads to a better agreement between the extracted resonance properties and those listed by PDG.

Acknowledgments

This work has been supported by the PUTI Q1 Grant of Universitas Indonesia, under contract No. BA-1080/UN2.RST/PPM.00.03.01/2020.

Appendix A: Form Functions A_i for Baryon Resonances with Spins 11/2, 13/2 and 15/2

The extracted form functions A_i given in Eq. (54) for baryon resonances with spin 11/2 read

$$\begin{aligned}
A_1 = & \left[14c_1 D_1 (s \pm m_{N^*} m_\Lambda) + 10D_3 \left\{ (m_\Lambda^2 c_k - b_p c_\Lambda) \pm m_{N^*} m_\Lambda \left(\frac{1}{s} c_k c_\Lambda - b_p \right) \right\} \right] G_1 \\
& + \frac{1}{2} (m_p + m_\Lambda) \left[\left\{ (m_p c_\Lambda - m_\Lambda c_p) \pm m_{N^*} (m_p m_\Lambda - \frac{1}{s} c_\Lambda c_p) \right\} \left\{ 28c_1 (c_1 - b_p c_s) D_4 - \frac{4}{s} k^2 c_2 c_p D_5 + D_3 \right\} \right. \\
& - b_p (m_\Lambda \pm \frac{1}{s} m_{N^*} c_\Lambda) D_3 \pm 7m_{N^*} \left\{ (c_1 - b_p c_s) D_2 - \frac{4}{s} k^2 c_1 c_2 c_p D_4 \right\} \left. \right] G_2 + \left[\frac{1}{2} (m_p + m_\Lambda) \left\{ (s \pm m_{N^*} m_p) \right. \right. \\
& \times \left\{ -7c_s D_2 - 4c_1 c_2 D_4 \frac{1}{s} c_k \right\} - \left\{ (m_p m_\Lambda + 11c_\Lambda) \pm m_{N^*} \left(\frac{1}{s} m_p c_\Lambda + 11m_\Lambda \right) \right\} D_3 \\
& - \left\{ (b_p c_\Lambda - m_p m_\Lambda c_k) \pm m_{N^*} \left(\frac{1}{s} m_p c_\Lambda c_k - m_\Lambda b_p \right) \right\} \left. \left(-28c_1 c_s D_4 - 4c_2 D_5 \frac{1}{s} c_k \right) \right\} \\
& + \left\{ (6m_p c_\Lambda + 6m_\Lambda c_p + m_\Lambda c_k) \pm m_{N^*} (6m_p m_\Lambda + \frac{6}{s} c_p c_\Lambda + \frac{1}{s} c_k c_\Lambda) \right\} D_3 \mp 7m_{N^*} c_1 D_1 \left. \right] G_3, \tag{A1}
\end{aligned}$$

$$\begin{aligned}
A_2 = & \frac{1}{t - m_K^2} \left\{ \left[-20k^2 D_3 (c_\Lambda \pm m_{N^*} m_\Lambda) \right] G_1 + \left[7(-s \pm m_{N^*} m_p) \left\{ (b_p c_s - c_1) D_2 + \frac{4}{s} k^2 c_1 c_2 c_p D_4 \right\} \right. \right. \\
& - m_p k^2 (m_\Lambda \pm \frac{1}{s} m_{N^*} c_\Lambda) D_3 + 4 \left\{ (m_p m_\Lambda c_k - b_p c_\Lambda) \pm m_{N^*} \left(\frac{1}{s} m_p c_\Lambda c_k - m_\Lambda b_p \right) \right\} \left. \left\{ 7c_1 D_4 (b_p c_s - c_1) \right. \right. \\
& + \left. \left. \frac{1}{s} k^2 c_2 c_p D_5 \right\} \right] G_2 + m_p \left[(m_\Lambda \pm \frac{1}{s} m_{N^*} c_\Lambda) \left\{ D_3 k^2 + 56c_1 c_k D_4 (c_1 - b_p c_s) - 8c_2 \frac{1}{s} k^2 c_k c_p D_5 \right\} \right. \\
& + \left. \left\{ (m_p c_\Lambda + m_\Lambda c_p) \pm m_{N^*} (m_p m_\Lambda + \frac{1}{s} c_\Lambda c_p) \right\} 4k^2 (7c_1 c_s D_4 + \frac{1}{s} c_2 c_k D_5) \right. \\
& \left. \pm 7m_{N^*} \left\{ D_2 (k^2 c_s - 2b_q) - 4c_1 c_2 k^2 D_4 (1 + \frac{1}{s} c_p) \right\} \right] G_3 \left. \right\}, \tag{A2}
\end{aligned}$$

$$\begin{aligned}
A_3 = & \left[10c_k D_3 (m_\Lambda \pm \frac{1}{s} m_{N^*} c_\Lambda) \pm 14m_{N^*} c_1 D_1 \right] G_1 + \frac{1}{2} \left[\left\{ (m_p c_\Lambda - m_\Lambda c_p) \pm m_{N^*} (m_p m_\Lambda - \frac{1}{s} c_\Lambda c_p) \right\} \right. \\
& \times \left\{ 28c_1 D_4 (c_1 + b_p (1 + \frac{1}{s} c_\Lambda)) - \frac{4}{s} k^2 c_2 c_p D_5 + D_3 \right\} - b_p (m_\Lambda \pm \frac{1}{s} m_{N^*} c_\Lambda) D_3 \\
& \left. \pm 7m_{N^*} \left\{ (c_1 + b_p (1 + \frac{1}{s} c_\Lambda)) D_2 - \frac{4}{s} k^2 c_1 c_2 c_p D_4 \right\} \right] G_2 + \frac{1}{2} \left[7(s \pm m_{N^*} m_p) \left\{ (1 + \frac{1}{s} c_\Lambda) D_2 - 4c_1 c_2 \frac{1}{s} c_k D_4 \right\} \right. \\
& - \left\{ (m_p m_\Lambda + 11c_\Lambda) \pm m_{N^*} \left(\frac{1}{s} m_p c_\Lambda + 11m_\Lambda \right) \right\} D_3 - \left\{ (b_p c_\Lambda - m_p m_\Lambda c_k) \pm m_{N^*} \left(\frac{1}{s} m_p c_\Lambda c_k - m_\Lambda b_p \right) \right\} \\
& \left. \times \left\{ 28c_1 D_4 (1 + \frac{1}{s} c_\Lambda) - 4c_2 D_5 \frac{1}{s} c_k \right\} \right] G_3, \tag{A3}
\end{aligned}$$

$$\begin{aligned}
A_4 = & \left[10c_k D_3 (m_\Lambda \pm \frac{1}{s} m_{N^*} c_\Lambda) \pm 14m_{N^*} c_1 D_2 \right] G_1 + \frac{1}{2} \left[\left\{ (m_p c_\Lambda - m_\Lambda c_p) \pm m_{N^*} (m_p m_\Lambda - \frac{1}{s} c_\Lambda c_p) \right\} \right. \\
& \times \left\{ 28c_1 D_4 (c_1 - b_p c_s) - \frac{4}{s} k^2 c_2 c_p D_5 + D_3 \right\} - b_p (m_\Lambda \pm \frac{1}{s} m_{N^*} c_\Lambda) D_3 \pm 7m_{N^*} \left\{ (c_1 - b_p c_s) D_2 \right. \\
& - \left. \frac{4}{s} k^2 c_1 c_2 c_p D_4 \right\} \left. \right] G_2 + \frac{1}{2} \left[7(s \pm m_{N^*} m_p) \left\{ -c_s D_2 - 4c_1 c_2 D_4 \frac{1}{s} c_k \right\} - \left\{ (m_p m_\Lambda + 11c_\Lambda) \right. \right. \\
& \left. \left. \pm m_{N^*} \left(\frac{1}{s} m_p c_\Lambda + 11m_\Lambda \right) \right\} D_3 - \left\{ (b_p c_\Lambda - m_p m_\Lambda c_k) \pm m_{N^*} \left(\frac{1}{s} m_p c_\Lambda c_k - m_\Lambda b_p \right) \right\} \right. \\
& \left. \times \left\{ -28c_1 c_s D_4 - 4c_2 D_5 \frac{1}{s} c_k \right\} \right] G_3, \tag{A4}
\end{aligned}$$

$$\begin{aligned}
A_5 = & \frac{1}{t - m_K^2} \left\{ \left[10c_5 D_3 (c_\Lambda \pm m_{N^*} m_\Lambda) \right] G_1 + \frac{1}{2} \left[7(-s \pm m_{N^*} m_p) \left\{ D_2 (b_p + b_\Lambda - \frac{1}{s} c_\Lambda c_5) - \frac{4}{s} c_1 c_2 c_5 c_p D_4 \right\} \right. \right. \\
& + m_p c_5 (m_\Lambda \pm \frac{1}{s} m_{N^*} c_\Lambda) D_3 + 4 \left\{ (m_p m_\Lambda c_k - b_p c_\Lambda) \pm m_{N^*} \left(\frac{1}{s} m_p c_\Lambda c_k - m_\Lambda b_p \right) \right\} \left. \left\{ 7c_1 D_4 (b_p + b_\Lambda - \frac{1}{s} c_\Lambda c_5) \right. \right. \\
& - \left. \left. \frac{1}{s} c_2 c_5 c_p D_5 \right\} \right] G_2 + m_p \left[-\frac{1}{2} (m_\Lambda \pm \frac{1}{s} m_{N^*} c_\Lambda) \left\{ c_5 \left\{ D_3 - \frac{8}{s} c_2 c_k c_p D_5 \right\} + 56c_1 c_k D_4 (b_p + b_\Lambda - \frac{1}{s} c_\Lambda c_5) \right\} \right. \\
& - \left. \left\{ (m_p c_\Lambda + m_\Lambda c_p) \pm m_{N^*} (m_p m_\Lambda + \frac{1}{s} c_\Lambda c_p) \right\} \left\{ 28c_1 D_4 (4b_\Lambda - k^2 - \frac{1}{s} c_\Lambda c_5) + \frac{4}{s} c_2 c_5 c_k D_5 \right\} \right. \\
& \left. \pm \frac{7}{2} m_{N^*} \left\{ D_2 (k^2 - 2b_q + \frac{1}{s} c_\Lambda c_5) + 4c_1 c_2 c_5 D_4 (1 + \frac{1}{s} c_p) \right\} \right] G_3 \left. \right\}, \tag{A5}
\end{aligned}$$

$$\begin{aligned}
A_6 = & \left[10 \left\{ (m_\Lambda s + m_p c_\Lambda) \pm m_{N^*} (c_\Lambda + m_p m_\Lambda) \right\} D_3 \right] G_1 + \frac{1}{2} \left[\left\{ (m_p c_\Lambda - m_\Lambda c_p) \pm m_{N^*} (m_p m_\Lambda - \frac{1}{s} c_\Lambda c_p) \right\} \right. \\
& \times \left\{ D_3 + 28c_1 D_4 (c_1 + b_p c_s) - \frac{4}{s} c_2 c_4 c_p D_5 \right\} + b_p (m_\Lambda \pm \frac{1}{s} m_{N^*} c_\Lambda) D_3 \\
& \left. \pm 7m_{N^*} \left\{ D_2 (c_1 + b_p c_s) - \frac{4}{s} c_1 c_2 c_4 c_p D_4 \right\} \right] G_2 + \frac{1}{2} m_p \left[7(s \pm m_{N^*} m_p) \left\{ D_2 c_s - 4c_1 c_2 D_4 (1 + \frac{1}{s} c_p) \right\} \right. \\
& + D_3 \left\{ (m_p m_\Lambda - 9c_\Lambda) \pm m_{N^*} \left(\frac{1}{s} m_p c_\Lambda - 9m_\Lambda \right) \right\} + 4 \left\{ 7c_1 c_s D_4 + c_2 D_5 (1 + \frac{1}{s} c_p) \right\} \left. \left\{ (m_p m_\Lambda c_k - b_p c_\Lambda) \right. \right. \\
& \left. \left. \pm m_{N^*} \left(\frac{1}{s} m_p c_\Lambda c_k - m_\Lambda b_p \right) \right\} \right] G_3, \tag{A6}
\end{aligned}$$

whereas the extracted functions A_i for baryon resonances with spin 13/2 read

$$\begin{aligned}
A_1 = & \left[2D_6(-s \pm m_{N^*}m_\Lambda) + 12c_1D_7\left\{- (m_\Lambda^2c_k - b_p c_\Lambda) \pm m_{N^*}m_\Lambda\left(\frac{1}{s}c_k c_\Lambda - b_p\right)\right\} \right] G_1 \\
& + \frac{1}{2}(m_p + m_\Lambda) \left[\left\{ -(m_p c_\Lambda - m_\Lambda c_p) \pm m_{N^*}(m_p m_\Lambda - \frac{1}{s}c_\Lambda c_p) \right\} \left\{ 5D_2(c_1 - b_p c_s) - \frac{20}{s}k^2c_1c_2c_pD_4 + c_1D_8 \right\} \right. \\
& - b_p(-m_\Lambda \pm \frac{1}{s}m_{N^*}c_\Lambda)c_1D_8 \pm m_{N^*} \left\{ 3c_1(c_1 - b_p c_s)D_9 - \frac{5}{s}k^2c_2c_pD_2 \right\} \left. \right] G_2 + \left[\frac{1}{2}(m_p + m_\Lambda) \right. \\
& \times \left\{ (-s \pm m_{N^*}m_p) \left\{ -3c_s c_1D_9 - 5\frac{1}{s}c_2c_kD_2 \right\} - c_1 \left\{ -(m_p m_\Lambda + 13c_\Lambda) \pm m_{N^*}(\frac{1}{s}m_p c_\Lambda + 13m_\Lambda) \right\} D_8 \right. \\
& + 5 \left\{ -(b_p c_\Lambda - m_p m_\Lambda c_k) \pm m_{N^*}(\frac{1}{s}m_p c_\Lambda c_k - m_\Lambda b_p) \right\} (c_s c_1^2 D_2 + \frac{4}{s}c_1c_2c_kD_4) \left. \right\} \\
& + c_1 \left\{ -(7m_p c_\Lambda + 7m_\Lambda c_p + m_\Lambda c_k) \pm m_{N^*}(7m_p m_\Lambda + \frac{7}{s}c_p c_\Lambda + \frac{1}{s}c_k c_\Lambda) \right\} D_8 \mp m_{N^*}D_6 \left. \right] G_3, \tag{A7}
\end{aligned}$$

$$\begin{aligned}
A_2 = & \frac{1}{t - m_K^2} \left\{ \left[-24k^2c_1D_7(-c_\Lambda \pm m_{N^*}m_\Lambda) \right] G_1 + \left[(s \pm m_{N^*}m_p) \left\{ 3c_1(b_p c_s - c_1)D_9 + \frac{5}{s}k^2c_2c_pD_2 \right\} \right. \right. \\
& - m_p k^2c_1(-m_\Lambda \pm \frac{1}{s}m_{N^*}c_\Lambda)D_8 + \left. \left\{ -(m_p m_\Lambda c_k - b_p c_\Lambda) \pm m_{N^*}(\frac{1}{s}m_p c_\Lambda c_k - m_\Lambda b_p) \right\} \left\{ 5D_2(b_p c_s - c_1) \right. \right. \\
& + \left. \left. \frac{20}{s}k^2c_1c_2c_pD_4 \right\} \right] G_2 + m_p \left[(-m_\Lambda \pm \frac{1}{s}m_{N^*}c_\Lambda) \left\{ k^2c_1D_8 + 10c_k(c_1 - b_p c_s)D_2 - \frac{40}{s}k^2c_1c_2c_kc_pD_4 \right\} \right. \\
& + \left. \left\{ -(m_p c_\Lambda + m_\Lambda c_p) \pm m_{N^*}(m_p m_\Lambda + \frac{1}{s}c_\Lambda c_p) \right\} 5k^2(c_s D_2 + \frac{4}{s}c_1c_2c_kD_4) \right. \\
& \left. \pm m_{N^*} \left\{ 3c_1D_9(k^2c_s - 2b_q) - 5k^2c_2(1 + \frac{1}{s}c_p)D_2 \right\} \right] G_3 \left. \right\}, \tag{A8}
\end{aligned}$$

$$\begin{aligned}
A_3 = & \left[12c_k c_1 D_7(-m_\Lambda \pm \frac{1}{s}m_{N^*}c_\Lambda) \pm 2m_{N^*}D_6 \right] G_1 + \frac{1}{2} \left[\left\{ -(m_p c_\Lambda - m_\Lambda c_p) \pm m_{N^*}(m_p m_\Lambda - \frac{1}{s}c_\Lambda c_p) \right\} \right. \\
& \times \left\{ 5D_2 + c_2^2 c_3^2 \right\} (c_1 + b_p(1 + \frac{1}{s}c_\Lambda)) - \frac{20}{s}k^2c_1c_2c_pD_4 + c_1D_2 \left. \right\} - b_p c_1(-m_\Lambda \pm \frac{1}{s}m_{N^*}c_\Lambda)D_8 \\
& \pm m_{N^*} \left\{ 3c_1(c_1 + b_p(1 + \frac{1}{s}c_\Lambda))D_9 - \frac{5}{s}k^2c_2c_pD_2 \right\} \left. \right] G_2 + \frac{1}{2} \left[(-s \pm m_{N^*}m_p) \left\{ 3c_1(1 + \frac{1}{s}c_\Lambda)D_9 \right. \right. \\
& - \frac{5}{s}c_2c_kD_2 \left. \right\} - c_1 \left\{ -(m_p m_\Lambda + 13c_\Lambda) \pm m_{N^*}(\frac{1}{s}m_p c_\Lambda + 13m_\Lambda) \right\} D_8 - 5 \left\{ -(b_p c_\Lambda - m_p m_\Lambda c_k) \right. \\
& \left. \pm m_{N^*}(\frac{1}{s}m_p c_\Lambda c_k - m_\Lambda b_p) \right\} \left\{ (1 + \frac{1}{s}c_\Lambda)D_2 - \frac{4}{s}c_1c_2c_kD_4 \right\} \left. \right] G_3, \tag{A9}
\end{aligned}$$

$$\begin{aligned}
A_4 = & \left[12c_k c_1 D_7(-m_\Lambda \pm \frac{1}{s}m_{N^*}c_\Lambda) \pm 2m_{N^*}D_6 \right] G_1 + \frac{1}{2} \left[\left\{ -(m_p c_\Lambda - m_\Lambda c_p) \pm m_{N^*}(m_p m_\Lambda - \frac{1}{s}c_\Lambda c_p) \right\} \right. \\
& \times \left\{ 5D_2(c_1 - b_p c_s) - \frac{20}{s}k^2c_1c_2c_pD_4 + c_1D_8 \right\} - b_p c_1(-m_\Lambda \pm \frac{1}{s}m_{N^*}c_\Lambda)D_8 \pm m_{N^*} \left\{ 3c_1(c_1 - b_p c_s)D_9 \right. \\
& - \left. \frac{5}{s}k^2c_2c_pD_2 \right\} \left. \right] G_2 + \frac{1}{2} \left[(-s \pm m_{N^*}m_p) \left\{ -3c_1c_sD_9 - \frac{5}{s}c_2c_kD_2 \right\} - c_1 \left\{ -(m_p m_\Lambda + 13c_\Lambda) \right. \right. \\
& \left. \pm m_{N^*}(\frac{1}{s}m_p c_\Lambda 13m_\Lambda) \right\} D_8 - 5 \left\{ -(b_p c_\Lambda - m_p m_\Lambda c_k) \pm m_{N^*}(\frac{1}{s}m_p c_\Lambda c_k - m_\Lambda b_p) \right\} \\
& \times (-c_s D_2 - \frac{4}{s}c_1c_2c_kD_4) \left. \right] G_3, \tag{A10}
\end{aligned}$$

$$\begin{aligned}
A_5 = & \frac{1}{t - m_K^2} \left\{ \left[12c_5c_1D_7\{-c_\Lambda \pm m_{N^*}m_\Lambda\} \right] G_1 + \frac{1}{2} \left[(s \pm m_{N^*}m_p) \left\{ 3c_1(b_p + b_\Lambda - \frac{1}{s}c_\Lambda c_5)D_9 - \frac{5}{s}c_2c_5c_pD_2 \right\} \right. \right. \\
& + m_p c_5 c_1(-m_\Lambda \pm \frac{1}{s}m_{N^*}c_\Lambda)D_8 + \left. \left\{ -(m_p m_\Lambda c_k - b_p c_\Lambda) \pm m_{N^*}(\frac{1}{s}m_p c_\Lambda c_k - m_\Lambda b_p) \right\} \right. \\
& \times \left. \left\{ 3c_1D_9(b_p + b_\Lambda - \frac{1}{s}c_\Lambda c_5) - \frac{20}{s}c_1c_2c_5c_pD_4 \right\} \right] G_2 + m_p \left[(m_\Lambda \mp \frac{1}{s}m_{N^*}c_\Lambda) \left\{ \frac{1}{2}c_1c_5D_8 \right. \right. \\
& + 10c_kD_2(b_p + b_\Lambda - \frac{1}{s}c_\Lambda c_5) + 20c_1c_2c_5D_4\frac{1}{s}c_p c_k \left. \right\} + \frac{5}{2} \left\{ (m_p c_\Lambda + m_\Lambda c_p) \mp m_{N^*}(m_p m_\Lambda + \frac{1}{s}c_\Lambda c_p) \right\} \\
& \times \left\{ (4b_\Lambda - k^2 - \frac{1}{s}c_\Lambda c_5)D_2 + 4c_1c_2c_5\frac{1}{s}c_kD_4 \right\} \pm \frac{1}{2}m_{N^*} \left\{ 3c_1D_9(k^2 - 2b_q + \frac{1}{s}c_\Lambda c_5) \right. \\
& \left. + 5c_2c_5D_2(1 + \frac{1}{s}c_p) \right\} \left. \right] G_3 \left. \right\}, \tag{A11}
\end{aligned}$$

$$\begin{aligned}
A_6 = & \left[12c_1 \left\{ -(m_\Lambda s + m_p c_\Lambda) \pm m_{N^*}(c_\Lambda + m_p m_\Lambda) \right\} D_7 \right] G_1 + \frac{1}{2} \left[\left\{ -(m_p c_\Lambda - m_\Lambda c_p) \pm m_{N^*}(m_p m_\Lambda - \frac{1}{s}c_\Lambda c_p) \right\} \right. \\
& \times \left\{ c_1D_8 + 5D_2(c_1 + b_p c_s) - \frac{20}{s}c_1c_2c_4c_pD_4 \right\} + b_p(-m_\Lambda \pm \frac{1}{s}m_{N^*}c_\Lambda)c_1D_8 \pm m_{N^*} \left\{ 3c_1(c_1 + b_p c_s)D_9 \right. \\
& - \left. \frac{5}{s}c_2c_4c_pD_2 \right\} \left. \right] G_2 + \frac{1}{2}m_p \left[(-s \pm m_{N^*}m_p) \left\{ 3c_1D_9c_s - 5c_2D_2(1 + \frac{1}{s}c_p) \right\} - c_1D_8 \left\{ (m_p m_\Lambda - 11c_\Lambda) \right. \right. \\
& \mp m_{N^*}(\frac{1}{s}m_p c_\Lambda - 11m_\Lambda) \left. \right\} + \left\{ 5D_2c_s - 20c_1c_2D_4(1 + \frac{1}{s}c_p) \right\} \\
& \times \left. \left\{ (b_p c_\Lambda - m_p m_\Lambda c_k) \pm m_{N^*}(\frac{1}{s}m_p c_\Lambda c_k - m_\Lambda b_p) \right\} \right] G_3, \tag{A12}
\end{aligned}$$

where we have defined

$$D_1 = 33c_1^4 + 30c_1^2c_2c_3 + 11c_2^2c_3^2, \quad (\text{A13})$$

$$D_2 = 33c_1^4 + 18c_1^2c_2c_3 + c_2^2c_3^2, \quad (\text{A14})$$

$$D_3 = 21c_1^4 + 14c_1^2c_2c_3 + c_2^2c_3^2, \quad (\text{A15})$$

$$D_4 = 3c_1^2 + c_2c_3, \quad (\text{A16})$$

$$D_5 = 7c_1^2 + c_2c_3, \quad (\text{A17})$$

$$D_6 = 429c_1^6 + 5(99c_1^4c_2c_3 + 27c_1^2c_2^2c_3^2 + c_2^3c_3^3), \quad (\text{A18})$$

$$D_7 = 33c_1^4 + 45c_1^2c_2c_3 + 5c_2^2c_3^2, \quad (\text{A19})$$

$$D_8 = 33c_1^4 + 120c_1^2c_2c_3 + 5c_2^2c_3^2, \quad (\text{A20})$$

$$D_9 = 143c_1^4 + 110c_1^2c_2c_3 + 15c_2^2c_3^2, \quad (\text{A21})$$

while c_1, c_2, c_3 and other parameters are defined in Eq. (53).

Finally, the extracted functions A_i for baryon resonances with spin 15/2 read

$$\begin{aligned} A_1 = & \left[\left(12879c_1^7 + 126c_1F_6 \right) (s \pm m_{N^*}m_\Lambda) + \left(14F_3 + 60c_2^3c_3^3 \right) \left\{ (m_\Lambda^2c_k - b_p c_\Lambda) \pm m_{N^*}m_\Lambda \left(\frac{1}{s}c_k c_\Lambda - b_p \right) \right\} \right] G_1 \\ & + \frac{1}{2}(m_p + m_\Lambda) \left[\left\{ (m_p c_\Lambda - m_\Lambda c_p) \pm m_{N^*} (m_p m_\Lambda - \frac{1}{s}c_\Lambda c_p) \right\} \left\{ F_4 (c_1 - b_p c_s) - \frac{1}{s}k^2 F_5 c_p + F_3 \right\} \right. \\ & \left. - b_p (m_\Lambda \pm \frac{1}{s}m_{N^*}c_\Lambda) F_3 \pm m_{N^*} \left\{ (c_1 - b_p c_s) F_1 - \frac{1}{s}k^2 F_2 c_p \right\} \right] G_2 \\ & + \left[\frac{1}{2}(m_p + m_\Lambda) \left\{ (s \pm m_{N^*}m_p) \left\{ -c_s F_1 - \frac{1}{s}c_k F_2 \right\} - \left\{ (m_p m_\Lambda + 15c_\Lambda) \pm m_{N^*} \left(\frac{1}{s}m_p c_\Lambda + 15m_\Lambda \right) \right\} F_3 \right. \right. \\ & \left. \left. - \left\{ (b_p c_\Lambda - m_p m_\Lambda c_k) \pm m_{N^*} \left(\frac{1}{s}m_p c_\Lambda c_k - m_\Lambda b_p \right) \right\} \left(-F_4 c_s - \frac{1}{s}c_k F_5 \right) \right\} \right. \\ & \left. + \left\{ (8m_p c_\Lambda + 8m_\Lambda c_p + m_\Lambda c_k) \pm m_{N^*} (8m_p m_\Lambda + \frac{8}{s}c_p c_\Lambda + \frac{1}{s}c_k c_\Lambda) \right\} F_3 \mp m_{N^*} c_1 F_1 \right] G_3, \quad (\text{A22}) \end{aligned}$$

$$\begin{aligned} A_2 = & \frac{1}{t - m_K^2} \left\{ \left[-4k^2 \left(7F_3 + 30c_2^3c_3^3 \right) (c_\Lambda \pm m_{N^*}m_\Lambda) \right] G_1 + \left[(-s \pm m_{N^*}m_p) \left\{ (b_p c_s - c_1) F_1 + \frac{1}{s}k^2 c_p F_2 \right\} \right. \right. \\ & \left. \left. - m_p k^2 (m_\Lambda \pm \frac{1}{s}m_{N^*}c_\Lambda) F_3 + \left\{ (m_p m_\Lambda c_k - b_p c_\Lambda) \pm m_{N^*} \left(\frac{1}{s}m_p c_\Lambda c_k - m_\Lambda b_p \right) \right\} \right] \right. \\ & \left. \times \left\{ F_4 (b_p c_s - c_1) + \frac{1}{s}k^2 c_p F_5 \right\} \right] G_2 + m_p \left[(m_\Lambda \pm \frac{1}{s}m_{N^*}c_\Lambda) \left\{ F_3 k^2 + 2c_k F_4 (c_1 - b_p c_s) \right. \right. \\ & \left. \left. - \frac{1}{s}k^2 2c_k c_p F_5 \right\} + \left\{ (m_p c_\Lambda + m_\Lambda c_p) \pm m_{N^*} (m_p m_\Lambda + \frac{1}{s}c_\Lambda c_p) \right\} k^2 (c_s F_4 + \frac{1}{s}c_k F_5) \right. \\ & \left. \pm m_{N^*} \left\{ F_1 (k^2 c_s - 2b_q) - F_3 k^2 (1 + \frac{1}{s}c_p) \right\} \right] G_3, \quad (\text{A23}) \end{aligned}$$

$$\begin{aligned} A_3 = & \left[2c_k \left(7F_3 + 30c_2^3c_3^3 \right) (m_\Lambda \pm \frac{1}{s}m_{N^*}c_\Lambda) \pm 2m_{N^*} (6435c_1^7 + 63c_1F_6) \right] G_1 \\ & + \frac{1}{2} \left[\left\{ (m_p c_\Lambda - m_\Lambda c_p) \pm m_{N^*} (m_p m_\Lambda - \frac{1}{s}c_\Lambda c_p) \right\} \left\{ F_4 (c_1 + b_p (1 + \frac{1}{s}c_\Lambda)) - \frac{1}{s}k^2 c_p F_5 + F_3 \right\} \right. \\ & \left. - b_p (m_\Lambda \pm \frac{1}{s}m_{N^*}c_\Lambda) F_3 \pm m_{N^*} \left\{ (c_1 + b_p (1 + \frac{1}{s}c_\Lambda)) F_1 - \frac{1}{s}k^2 c_p F_2 \right\} \right] G_2 \\ & + \frac{1}{2} \left[(s \pm m_{N^*}m_p) \left\{ (1 + \frac{1}{s}c_\Lambda) F_1 - F_2 \frac{1}{s}c_k \right\} - \left\{ (m_p m_\Lambda + 15c_\Lambda) \pm m_{N^*} \left(\frac{1}{s}m_p c_\Lambda + 15m_\Lambda \right) \right\} F_3 \right. \\ & \left. - \left\{ (b_p c_\Lambda - m_p m_\Lambda c_k) \pm m_{N^*} \left(\frac{1}{s}m_p c_\Lambda c_k - m_\Lambda b_p \right) \right\} \left\{ F_4 (1 + \frac{1}{s}c_\Lambda) - F_5 \frac{1}{s}c_k \right\} \right] G_3, \quad (\text{A24}) \end{aligned}$$

$$\begin{aligned} A_4 = & \left[2c_k \left(7F_3 + 30c_2^3c_3^3 \right) (m_\Lambda \pm \frac{1}{s}m_{N^*}c_\Lambda) \pm 2m_{N^*} (6435c_1^7 + 63c_1F_6) \right] G_1 \\ & + \frac{1}{2} \left[\left\{ (m_p c_\Lambda - m_\Lambda c_p) \pm m_{N^*} (m_p m_\Lambda - \frac{1}{s}c_\Lambda c_p) \right\} \left\{ F_4 (c_1 - b_p c_s) - \frac{1}{s}k^2 c_p F_5 + (5c_1^2 + c_2c_3) \right\} \right. \\ & \left. - b_p (m_\Lambda \pm \frac{1}{s}m_{N^*}c_\Lambda) F_3 \pm m_{N^*} \left\{ (c_1 - b_p c_s) F_1 - \frac{1}{s}k^2 c_p F_2 \right\} \right] G_2 \\ & + \frac{1}{2} \left[(s \pm m_{N^*}m_p) \left(-c_s F_1 - F_2 \frac{1}{s}c_k \right) - \left\{ (m_p m_\Lambda + 15c_\Lambda) \pm m_{N^*} \left(\frac{1}{s}m_p c_\Lambda + 15m_\Lambda \right) \right\} F_3 \right. \\ & \left. - \left\{ (b_p c_\Lambda - m_p m_\Lambda c_k) \pm m_{N^*} \left(\frac{1}{s}m_p c_\Lambda c_k - m_\Lambda b_p \right) \right\} \left(-c_s F_4 - F_5 \frac{1}{s}c_k \right) \right] G_3, \quad (\text{A25}) \end{aligned}$$

$$\begin{aligned}
A_5 = & \frac{1}{t - m_K^2} \left\{ \left[2c_5(7F_3 + 30c_2^3c_3^3)(c_\Lambda \pm m_{N^*}m_\Lambda) \right] G_1 + \frac{1}{2} \left[(-s \pm m_{N^*}m_p) \left\{ F_1(b_p + b_\Lambda - \frac{1}{s}c_\Lambda c_5) - \frac{1}{s}c_5c_p F_2 \right\} \right. \right. \\
& + m_p c_5 (m_\Lambda \pm \frac{1}{s}m_{N^*}c_\Lambda) F_3 + \left. \left\{ (m_p m_\Lambda c_k - b_p c_\Lambda) \pm m_{N^*} (\frac{1}{s}m_p c_\Lambda c_k - m_\Lambda b_p) \right\} \left\{ F_4(b_p + b_\Lambda - \frac{1}{s}c_\Lambda c_5) \right. \right. \\
& \left. \left. - \frac{1}{s}c_p c_5 F_5 \right\} \right] G_2 + m_p \left[-\frac{1}{2} (m_\Lambda \pm \frac{1}{s}m_{N^*}c_\Lambda) \left\{ c_5(F_3 - \frac{1}{s}c_p c_k F_5) + c_k F_4(b_p + b_\Lambda - \frac{1}{s}c_\Lambda c_5) \right\} \right. \\
& \left. - \left\{ (m_p c_\Lambda + m_\Lambda c_p) \pm m_{N^*} (m_p m_\Lambda + \frac{1}{s}c_\Lambda c_p) \right\} \left\{ F_4(4b_\Lambda - k^2 - \frac{1}{s}c_\Lambda c_5) + \frac{1}{s}c_k c_5 F_5 \right\} \right. \\
& \left. \pm \frac{1}{2} m_{N^*} \left\{ F_1(k^2 - 2b_q + \frac{1}{s}c_\Lambda c_5) + c_5 F_2(1 + \frac{1}{s}c_p) \right\} \right] G_3 \Big\}, \tag{A26}
\end{aligned}$$

$$\begin{aligned}
A_6 = & \left[2 \left\{ (m_\Lambda s + m_p c_\Lambda) \pm m_{N^*} (c_\Lambda + m_p m_\Lambda) \right\} (7F_3 + 30c_2^3c_3^3) \right] G_1 \\
& + \frac{1}{2} \left[\left\{ (m_p c_\Lambda - m_\Lambda c_p) \pm m_{N^*} (m_p m_\Lambda - \frac{1}{s}c_\Lambda c_p) \right\} \left\{ F_3 + F_4(c_1 + b_p c_s) - \frac{1}{s}c_p c_4 F_5 \right\} \right. \\
& \left. + b_p (m_\Lambda \pm \frac{1}{s}m_{N^*}c_\Lambda) F_3 \pm m_{N^*} \left\{ F_1(c_1 + b_p c_s) - \frac{1}{s}c_4 c_p F_2 \right\} \right] G_2 \\
& + \frac{1}{2} m_p \left[(s \pm m_{N^*}m_p) \left\{ F_1 c_s - F_2(1 + \frac{1}{s}c_p) \right\} + F_3 \left\{ (m_p m_\Lambda - 11c_\Lambda) \pm m_{N^*} (\frac{1}{s}m_p c_\Lambda - 11m_\Lambda) \right\} \right. \\
& \left. + \left\{ c_s F_4 + F_5(1 + \frac{1}{s}c_p) \right\} \left\{ (m_p m_\Lambda c_k - b_p c_\Lambda) \pm m_{N^*} (\frac{1}{s}m_p c_\Lambda c_k - m_\Lambda b_p) \right\} \right] G_3, \tag{A27}
\end{aligned}$$

where in terms of c_1, c_2 , and c_3 defined in Eq. (53) we have used

$$F_1 = 45(143c_1^6 + 143c_1^4c_2c_3 + 33c_1^2c_2^2c_3^2 + c_2^3c_3^3), \tag{A28}$$

$$F_2 = 9c_1c_2(286c_1^4 + 220c_1^2c_2c_3 + 30c_2^2c_3^2), \tag{A29}$$

$$F_3 = 429c_1^6 + 495c_1^4c_2c_3 + 135c_1^2c_2^2c_3^2, \tag{A30}$$

$$F_4 = 18c_1(143c_1^4 + 110c_1^2c_2c_3 + 15c_2^2c_3^2), \tag{A31}$$

$$F_5 = 30c_2(33c_1^4 + 18c_1^2c_2c_3 + c_2^2c_3^2), \tag{A32}$$

$$F_6 = 143c_1^4c_2c_3 + 55c_1^2c_2^2c_3^2 + 5c_2^3c_3^3. \tag{A33}$$

-
- [1] S. Clymton and T. Mart, Phys. Rev. D **96**, 054004 (2017).
[2] V. Pascalutsa, Phys. Lett. B **503**, 85 (2001).
[3] T. Mart, Phys. Rev. D **100**, 056008 (2019).
[4] P. A. Zyla *et al.* [Particle Data Group], Prog. Theor. Exp. Phys. **2020**, 083C01 (2020).
[5] S. Clymton and T. Mart, JPS Conf. Proc. **26**, 031009 (2019).
[6] R. A. Adelseck and B. Saghai, Phys. Rev. C **42**, 108 (1990).
[7] T. Vrancx, L. De Cruz, J. Ryckebusch and P. Van-
craeyveld, Phys. Rev. C **84**, 045201 (2011).
[8] N. H. Luthfiah and T. Mart, AIP Conf. Proc. **2234**,
040015 (2020).
[9] V. Pascalutsa, Phys. Rev. D **58**, 096002 (1998).
[10] V. Pascalutsa and R. Timmermans, Phys. Rev. C **60**,
042201 (1999).
[11] S. Z. Huang, P. F. Zhang, T. N. Ruan, Y. C. Zhu and
Z. P. Zheng, Commun. Theor. Phys. **41**, 405 (2004).
[12] B. Deo and A. Bisoi, Phys. Rev. D **9**, 288 (1974).
[13] P. Dennery, Phys. Rev. **124**, 2000 (1961).
[14] T. Mart, S. Clymton, and A. J. Arifi, Phys. Rev. D **92**,
094019 (2015).
[15] C. Akondi *et al.* [A2 Collaboration at MAMI], Eur. Phys.
J. A **55**, 202 (2019).
[16] R. Bradford *et al.* [CLAS Collaboration], Phys. Rev. C
73, 035202 (2006).
[17] T. Mart and C. Bennhold, Phys. Rev. C **61**, 012201
(1999).
[18] T. Mart and M. Kholili, Phys. Rev. C **86**, 022201 (2012).
[19] M. Sumihama *et al.* [LEPS Collaboration], Phys. Rev. C
73, 035214 (2006).
[20] M. McCracken *et al.* [CLAS Collaboration], Phys. Rev.
C **81**, 025201 (2010).
[21] T. Jude *et al.* [Crystal Ball Collaboration at MAMI],
Phys. Lett. B **735**, 112 (2014).
[22] T. Mart, C. Bennhold and C. E. Hyde, Phys. Rev. C **51**,
1074 (1995).
[23] T. Mart, Phys. Rev. C **83**, 048203 (2011).
[24] N. Compton *et al.* [CLAS Collaboration], Phys. Rev. C
96, 065201 (2017).
[25] A. Lleres *et al.* [GRAAL Collaboration], Eur. Phys. J. A
39, 149 (2009).
[26] R. Bradford *et al.* [CLAS Collaboration], Phys. Rev. C
75, 035205 (2007).
[27] C. Paterson *et al.* [CLAS Collaboration], Phys. Rev. C
93, 065201 (2016).
[28] T. Mart and M. Kholili, J. Phys. G **46**, 105112 (2019).
[29] S. Clymton and T. Mart, arXiv:2104.10333 [hep-ph],
Phys. Rev. D (accepted for publication 2021).
[30] J. McNabb *et al.* [CLAS Collaboration], Phys. Rev. C

- 69**, 042201 (2004).
- [31] B. Dey *et al.*, Phys. Rev. C **82**, 025202 (2010).
- [32] A. Lleres *et al.* [GRAAL Collaboration], Eur. Phys. J. A **31**, 79 (2007).
- [33] K. Glander *et al.* [SAPHIR Collaboration], Eur. Phys. J. A **19**, 251 (2004).
- [34] H. Kohri *et al.* [LEPS Collaboration], Phys. Rev. Lett. **97**, 082003 (2006).
- [35] R. Lawall *et al.* [SAPHIR Collaboration], Eur. Phys. J. A **24**, 275 (2005).
- [36] R. Castelijns *et al.* [CBELSA/TAPS Collaboration], Eur. Phys. J. A **35**, 39 (2008).
- [37] P. Aguar-Bartolomé *et al.* [A2 Collaboration at MAMI], Phys. Rev. C **88**, 044601 (2013).
- [38] T. Mart, Phys. Rev. C **90**, 065202 (2014).
- [39] S. Sakinah, S. Clymton and T. Mart, Acta Phys. Polon. B **50**, 1389 (2019).
- [40] S. Pereira *et al.* [CLAS Collaboration], Phys. Lett. B **688**, 289 (2010).
- [41] F. James and M. Roos, Comput. Phys. Commun. **10**, 343 (1975).